Hole doping dependent electronic instability and electron-phonon coupling in infinite-layer nickelates

Xuelei Sui,[1] Jianfeng Wang,[2] Chao Chen,[3] Xiang Ding,[4] Ke-Jin Zhou,[5] Chao Cao,[6,*] Liang Qiao,[4,†] Haiqing Lin,[6,1,3] and Bing Huang[1,3,‡]

[1]*Beijing Computational Science Research Center, Beijing 100193, China*
[2]*School of Physics, Beihang University, Beijing 100191, China*
[3]*Department of Physics, Beijing Normal University, Beijing 100875, China*
[4]*School of Physics, University of Electronic Science and Technology of China, Chengdu 610054, China*
[5]*Diamond Light Source, Harwell Campus, Didcot OX11 0DE, England, United Kingdom*
[6]*Center for Correlated Matter and School of Physics, Zhejing University, Hangzhou 310058, China*

(Received 12 February 2022; revised 17 December 2022; accepted 14 February 2023; published 28 February 2023)

Recently, charge density waves (CDWs) have been observed in $CaCuO_2$-analogous infinite-layer nickelates $RNiO_2$ (R = La, Nd) but exhibit very different hole doping dependent behaviors compared to that in cuprates, raising a challenging question on its origin. In this paper, employing density functional theory, many-body dynamic mean field theory, and determinant quantum Monte Carlo calculations, we propose a synergetic contribution from both electronic instability (EI) and moment-dependent electron-phonon coupling (MEPC). Unexpectedly, the EI and MEPC are mainly contributed by Ni $3d_{x2-y2}$ and R $5d_{z2}$, highlighting the unique multiorbital feature. Interestingly, a strong Fermi surface nesting (FSN) induced by the unique feature of van Hove singularity (VHS) across the Fermi level exists in $RNiO_2$, which is sensitive to hole doping. The hole doping can rapidly reduce FSN of Ni $3d_{x2-y2}$ by shifting VHS and decrease the occupation of R $5d_{z2}$, which can largely weaken EI and MEPC in $RNiO_2$. Remarkably, the temperature-insensitive feature of EI and MEPC could be a hint for rather high-temperature CDWs observed in undoped $RNiO_2$. Our theory may offer one possible explanation to the experimentally observed CDW formation and its hole-doping dependence in nickelates, and also establishes a unified understanding of the hole doping dependent EI and MEPC in nickelates and cuprates.

DOI: 10.1103/PhysRevB.107.075159

I. INTRODUCTION

Despite over 30 years of intense effort, the understandings of the physical origin accounting for the existence of high-temperature superconductivity [1–3] and competing symmetry-breaking orders [4,5] in cuprates remain the top questions in condensed matter physics. A possible route to solve the long-standing puzzles in cuprates is to find other non-Cu-based superconductors but with cuprate-analogous structures [6,7]. Recently, the long-awaited superconductivity was eventually realized in hole-doped infinite-layer nickelates [8–11], potentially bringing us to the new age of nickelates. However, at this stage, there are still many debates on the fundamental physical properties of nickelates, including whether the pairing mechanism of superconductivity in nickelates (with multiorbital feature) is similar to that in cuprates (with single-orbital feature) [12–16] and what is the role of electron correlation effect in nickelates [17,18].

Besides the superconductivity, charge density waves (CDWs), which are popular but competing or intertwining with superconductivity in cuprates [4,5,19,20], are also observed in $LaNiO_2$ [21] and $NdNiO_2$ [22,23] with similar stripe patterns. In cuprates, the CDWs are usually absent in undoped systems but appear under certain hole doping concentrations (n_h) with a dome shape [5,24]. Although there are still some debates [25–29], it is commonly believed that the strong electron/spin correlation effect plays a dominant role in generating CDWs and spin density waves in cuprates [30], as also indicated by some many-body approaches with numerical evidence of fluctuating stripes [31,32]. However, in nickelates, the CDWs appear in undoped $LaNiO_2$ [21] and $NdNiO_2$ [22,23] and are monotonously suppressed and eventually disappear without a dome as Sr-doping-induced n_h increases, accompanied by the shift of $\boldsymbol{q}_{\mathrm{CDW}}$ vector [21]. Differing from the quasi-two-dimensional (2D) feature in cuprates [4,5], the CDWs in nickelates show a three-dimensional (3D) feature with non-negligible out-of-plane dependence [22]. In addition, the soft optical modes are observed in $LaNiO_2$ accompanied by the CDW evolution [21], which indicates that the electron-phonon coupling (EPC) may play an important role in the CDW formation. Therefore, the different CDW features and different hole doping dependent evolutions in nickelates and cuprates raise a fundamental question on its origin.

In this paper, employing both the density functional theory (DFT) and dynamical mean field theory (DMFT) calculations, we propose a joint electronic instability (EI) and

*ccao@zju.edu.cn
†liang.qiao@uestc.edu.cn
‡bing.huang@csrc.ac.cn

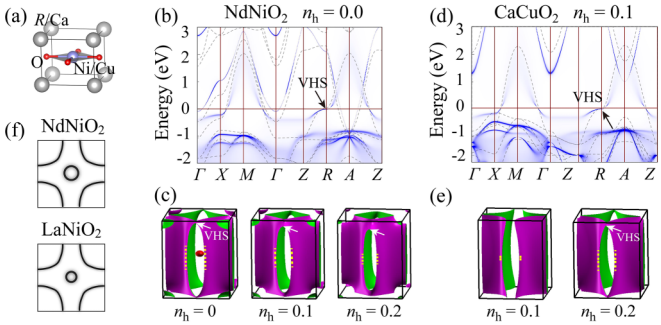

FIG. 1. (a) Crystal structure of RNiO$_2$ and CaCuO$_2$. (b), (c) DMFT-calculated (b) $\boldsymbol{k}$-resolved spectral function of pristine NdNiO$_2$ and (c) Fermi surface evolution of NdNiO$_2$ as a function of hole doping (in units of Sr/u.c.). (d), (e) DMFT-calculated (d) $\boldsymbol{k}$-resolved spectral function of 0.1h-doped CaCuO$_2$ and (e) Fermi surface evolution of CaCuO$_2$ as a function of hole doping (in units of hole/u.c.). In (b) and (d), black dashed lines are DFT-calculated band structures. Fermi level is set to zero. VHSs are labeled by arrows. Yellow-dashed lines in (c) and (e) highlight the parallel segments of FS evolutions along k_z. (f) DMFT-calculated cross sections of Fermi surfaces in the $k_z = 0$ plane for NdNiO$_2$ and LaNiO$_2$.

moment-dependent EPC (MEPC). This might be different from the common belief of the dominant role of electron effect on the CDW formation in cuprates. Remarkably, different from the low-energy single-orbital physics in CaCuO$_2$, the Ni $3d_{x2-y2}$ and R $5d_{z2}$ play a larger role in contribution to EI and MEPC. In particular, the van Hove singularity (VHS) near the Fermi level can induce strong Fermi surface nesting (FSN) at a series of k_z planes in undoped RNiO$_2$. As the n_h increases, the reduced FSN of Ni $3d_{x2-y2}$ due to the shift of VHS and the decreased occupation of R $5d_{z2}$ can gradually weaken the EI and MEPC in RNiO$_2$. These n_h-dependent behaviors of EI and MEPC in RNiO$_2$ are significantly different from those in CaCuO$_2$, due to the unique position of VHS and multiorbitals around E_F in RNiO$_2$. Surprisingly, both EI and MEPC are insensitive to the temperature, which may suggest a rather high-temperature CDW phase in undoped RNiO$_2$ up to 400 K.

II. HOLE DOPING DEPENDENT BAND STRUCTURES AND FERMI SURFACES

Figure 1(a) shows the unit cell structure of RNiO$_2$ and CaCuO$_2$. Since the RNiO$_2$ thin film is grown on SrTiO$_3$ (STO) substrate, its in-plane lattice constant is fixed to that of STO (3.905 Å) but its out-of-plane lattice constant is fully relaxed during the calculations. Meanwhile, because we focus on the mechanism of translational symmetry-breaking orders in nickelates, it is more appropriate to start from the state preserving translational symmetry, i.e., a paramagnetic (PM) state. The nonmagnetic (NM) state obtained from the DFT calculations can serve as an approximation of the PM state. In addition, the long-range antiferromagnetic (AFM) order cannot be stabilized in RNiO$_2$ either at the temperature of 116 K in our DMFT calculations or at a rather low temperature of 20 K in the experiments [33–37]. Figure 1(b) shows the comparison of DFT-calculated band structure (dashed line) in the NM state and the DMFT-calculated $\boldsymbol{k}$-resolved spectral function in the PM state for NdNiO$_2$. Overall, the DFT calculations can capture the major band dispersions obtained from the DMFT calculations, although the exact energy levels between these two methods are slightly different. The most noticeable difference between DFT and DMFT calculations in NdNiO$_2$ is the bandwidth of $3d_{x2-y2}$, which is largely reduced due to the many-body electron correlation effect induced

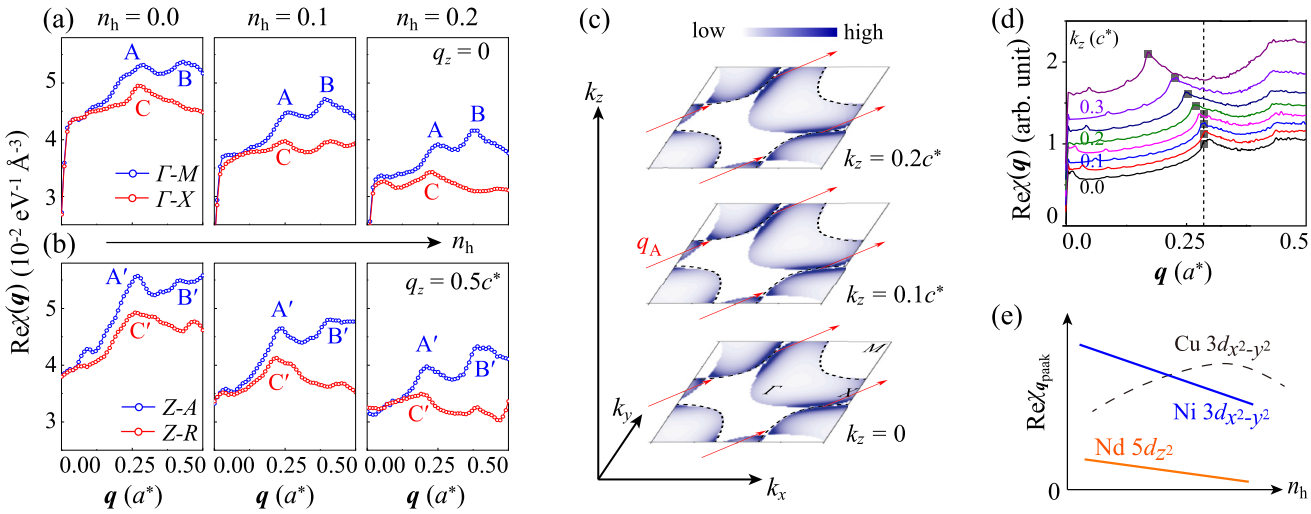

FIG. 2. (a) Static-QP Re$\chi(\boldsymbol{q})$ of NdNiO$_2$ under three different n_h (in units of Sr/u.c.) along two high-symmetry lines in the $q_z = 0$ plane. (b) Same as (a) but in the $q_z = 0.5c^*$ plane. $A(A')$, $B(B')$, and $C(C')$ indicate the corresponding peak positions in Re$\chi(\boldsymbol{q})$ at different $\boldsymbol{q}$. (c) Evolution of $\boldsymbol{k}$-resolved static-QP Re$\chi_{\boldsymbol{q}}(\boldsymbol{k})$ at $\boldsymbol{q}_A$ along different (small) k_z in undoped NdNiO$_2$, where Re$\chi_{\boldsymbol{q}}(\boldsymbol{k})$ is projected to the Ni $3d_{x2-y2}$ orbital. Black-dashed lines represent the FS of the Ni $3d_{x2-y2}$ band and red arrows of $\boldsymbol{q}_A$ connect the electronic states on FS to form a nesting (in view of almost unchanged FS along k_z). (d) Static-QP Re$\chi(\boldsymbol{q})$ along the Γ-M line for the $3d_{x2-y2}$ band in different k_z planes in undoped NdNiO$_2$. Peak positions of Re$\chi(\boldsymbol{q})$ in different k_z planes are labeled by black squares and the $\boldsymbol{q}_A$ position is highlighted by dashed lines, which indicate that the Re$\chi(\boldsymbol{q})$ in a small k_z (from 0 to 0.15c^*) can contributed to peak A. (e) Contributions of Ni $3d_{x2-y2}$ and Nd $5d_{z2}$ to Re$\chi_{\boldsymbol{q}\text{peak}}$ as a function of n_h. A schematic drawing of the contribution of Cu $3d_{x2-y2}$ to Re$\chi_{\boldsymbol{q}\text{peak}}$ of CaCuO$_2$ is also plotted here for comparison.

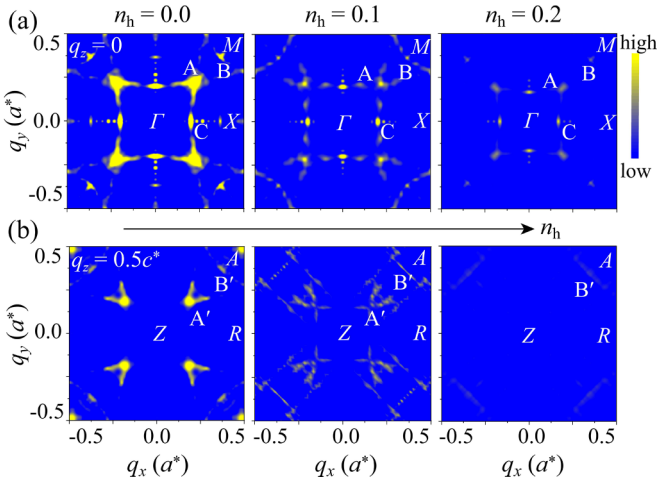

FIG. 3. (a) DFT-calculated $\boldsymbol{q}$-resolved $\gamma(\boldsymbol{q})$ under three different n_h (in units of Sr/u.c.) in the $q_z = 0$ plane from all phonon modes for electronic states in the entire BZ. (b) Same as (a) but in the $q_z = 0.5c^*$ plane. $A(A')$, $B(B')$, and $C(C')$ indicate the corresponding peak positions in $\gamma(\boldsymbol{q})$ at different $\boldsymbol{q}$, which are consistent with those in $\mathrm{Re}\chi(\boldsymbol{q})$.

band renormalization. Our DMFT spectral function results are consistent with previous DMFT studies on $R\mathrm{NiO_2}$ [38–42]. Interestingly, the VHSs at X and R points around the Fermi level in the band structures, which are mainly caused by the Lieb-type lattice of the $\mathrm{NiO_2}$ plane, are robust and insensitive to the many-body electron correlations. In addition, the basic band structure of $\mathrm{NdNiO_2}$ as well as the position of VHS are insensitive to the choice of lattice parameter (Fig. 6) and the Hubbard U (Fig. 7).

As shown in Fig. 1(d), a parallel study is also done for the case of $\mathrm{CaCuO_2}$. The ground state of parental $\mathrm{CaCuO_2}$ is an AFM insulator (Fig. 8). To better compare to the band structure of pristine $\mathrm{NdNiO_2}$, we present the $0.1h$-doped $\mathrm{CaCuO_2}$, where h denotes "hole," in which the magnetism is fully suppressed. It is known that the effect of electron correlation will be reduced in the Hubbard lattice if the electron occupation deviates from half filling [43–45]. But even under $0.1h$ doping, compared to the undoped $\mathrm{NdNiO_2}$, the band renormalization is still more noticeable in $\mathrm{CaCuO_2}$ after the inclusion of many-body electron correlations, not only for the $3d_{x2-y2}$ orbital across the Fermi level, but also for these states in the energy range of [–2, 0] eV. The calculated effective mass (m^*/m_0) of $3d_{x2-y2}$ is 3.52 (2.58) and 3.71 (2.43) for $0.1h$-doped and $0.2h$-doped $\mathrm{CaCuO_2}$ ($\mathrm{NdNiO_2}$), respectively. The VHS at the R point around Fermi level is insensitive to the many-body electron correlations in $\mathrm{CaCuO_2}$.

Another significant difference between $\mathrm{NdNiO_2}$ and $\mathrm{CaCuO_2}$ is the presence of the partially occupied low-lying R $5d_{z2}$ state across Fermi level in the $k_z = 0$ plane, which slightly hybridizes with the Ni $3d_{z2}$ orbital [13,46–50]. Importantly, in the undoped $\mathrm{NdNiO_2}$, the VHS is below Fermi level in the $k_z = 0$ plane but very close to Fermi level in the $k_z = 0.5c^*$ plane. However, differing from $R\mathrm{NiO_2}$, all the VHSs in $0.1h$-doped $\mathrm{CaCuO_2}$ are located below Fermi level, partially due to the absence of the Ca $5d_{z2}$ state around Fermi level induced over occupation of $3d_{x2-y2}$ in $\mathrm{CaCuO_2}$. As illustrated below, the different locations of VHSs in $\mathrm{NdNiO_2}$ and $\mathrm{CaCuO_2}$ will lead to a delicate difference in their FSs of the $3d_{x2-y2}$ band and corresponding EI.

The band structures of $\mathrm{NdNiO_2}$ and $\mathrm{CaCuO_2}$ as a function of Sr or hole doping are also calculated by DMFT method. For the case of $\mathrm{NdNiO_2}$ (Fig. 9), interestingly, we observe that the Sr doping gives rise to nonrigid shift of different orbitals, i.e., the electron pocket at the Γ point (induced by the Nd $5d$ orbital) is quickly suppressed while the electron pocket at the A point (induced by the interstitial s-like orbital) upshifts moderately, in agreement with the DFT results (Fig. 9) and previous DFT+DMFT calculations [41,51]. The Ni $3d_{x2-y2}$, the most correlated orbital, shifts upwards slightly upon Sr doping. For the case of $\mathrm{CaCuO_2}$ (Fig. 10), there is only one single Cu $3d_{x2-y2}$ band across the Fermi level, which shifts upwards slightly upon hole doping.

The calculated FS evolutions of $\mathrm{NdNiO_2}$ and $\mathrm{CaCuO_2}$ as a function of hole doping are shown in Figs. 1(c) and 1(e). In both systems, the $3d_{x2-y2}$ orbital shows a cylinderlike hole pocket, exhibiting a quasi-2D-like dispersion. Interestingly, we discover that the existence of VHS and its hole-doping dependence play a key role in determining the FS evolutions in both $\mathrm{NdNiO_2}$ and $\mathrm{CaCuO_2}$. For the undoped $\mathrm{NdNiO_2}$ [left panel, Fig. 1(c)], when k_z changes gradually from $0.5c^*$ to zero, near VHS [labeled by the arrow in Fig. 1(c)], there is a significant momentum variation of FS in the k_x-k_y plane; after passing through VHS, the energy band has a very large dispersion, and the shape of FS is almost unchanged in the k_x-k_y plane for small k_z, exhibiting a nearly parallel segment of FS [highlighted by parallel lines in Fig. 1(c)]. Importantly, as the n_h increases [from left to right, Fig. 1(c)], the VHS across Fermi level in $\mathrm{NdNiO_2}$ shifts to smaller k_z values, which reduces the k_z range for the parallel segment of FS of the Ni $3d_{x2-y2}$ band [i.e., the length of parallel lines in Fig. 1(c)]. Remarkably, the case is opposite for $\mathrm{CaCuO_2}$, due to the opposite n_h-dependent VHS evolution. As shown in Fig. 1(e), as hole doping increases, the VHS shifts closer to the Fermi level and eventually touches Fermi level around $n_h = 0.2h/u.c.$, where "u.c." denotes "unit cell." As a result, the parallel segment of FS of Cu $3d_{x2-y2}$ increases as the n_h increases. As we discussed in Sec. III, the evolution of parallel segments of FS of $3d_{x2-y2}$ plays a key role in determining the FSN strength in $R\mathrm{NiO_2}$ and $\mathrm{CaCuO_2}$. Another striking difference between $\mathrm{NdNiO_2}$ and $\mathrm{CaCuO_2}$ is the appearance of the Nd $5d_{z2}$ state in the vicinity of the Γ point [Fig. 1(b)], which forms a spherelike electron pocket in $\mathrm{NdNiO_2}$ [left panel, Fig. 1(c)], exhibiting an isotropic 3D dispersion.

In general, the hole-dependent band structure of $\mathrm{LaNiO_2}$ is similar to that of $\mathrm{NdNiO_2}$. The major difference between $\mathrm{LaNiO_2}$ and $\mathrm{NdNiO_2}$ is the size of the electron pocket at the Γ point. Since the orbital energy of La $5d$ is higher than that of Nd $5d$, fewer $5d_{z2}$ orbitals are occupied in $\mathrm{LaNiO_2}$ than in $\mathrm{NdNiO_2}$, resulting in a smaller electron pocket in $\mathrm{LaNiO_2}$ [Fig. 1(f)]. As discussed in Sec. VI, this difference will result in weaker EI and MEPC in $\mathrm{LaNiO_2}$ than in $\mathrm{NdNiO_2}$.

III. HOLE DOPING DEPENDENT EI

Differing from the AFM Mott insulating ground state of $\mathrm{CaCuO_2}$ [52–54], only local AFM fluctuations (magnon) are

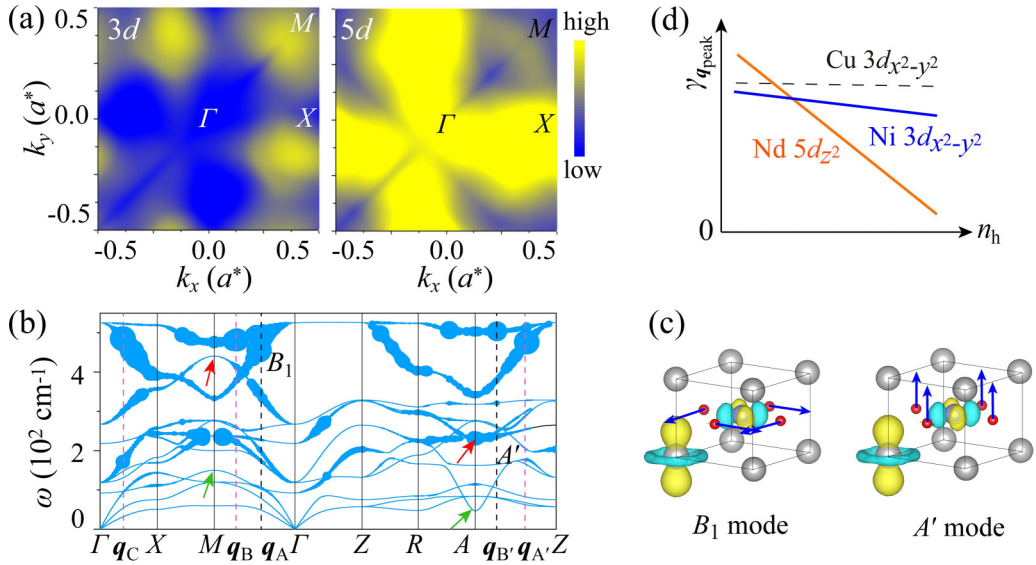

FIG. 4. (a) DFT-calculated MEPC matrix $g(\boldsymbol{k})$ for $3d_{x2-y2}$ (left panel) and $5d_{z2}$ (right panel) from all the phonon modes at $\boldsymbol{q}_A$ in the $k_z = 0$ plane. (b) DFT-calculated phonon spectrum of undoped $NdNiO_2$ with the magnitudes of phonon linewidth indicated by the line thickness. (c) Two typical strong orbital-phonon coupling modes at $\boldsymbol{q}_A$ (left) and $\boldsymbol{q}''_B$ (right). (d) Contributions of Ni $3d_{x2-y2}$ and Nd $5d_{z2}$ to $\gamma_{\boldsymbol{q}\text{peak}}$ as functions of n_h. The contribution of Cu $3d_{x2-y2}$ to $\gamma_{\boldsymbol{q}\text{peak}}$ of $CaCuO_2$ is also plotted.

observed in nickelates at rather low temperature [34–36], which cannot coexist with the CDW phases in $NdNiO_2$ [21,22], due to the competing for energy gain between these different symmetry-breaking orders [4]. Meanwhile, although moderate hole doping can introduce superconductivity in both $CaCuO_2$ and $RNiO_2$, it could stabilize the CDW phases in $CaCuO_2$ [4,5] but weakens or even destroys the CDW phases in $RNiO_2$ [21,22]. It is expected that the different low-energy orbital feature and different hole doping dependent FS evolution might play some roles in accounting for the different CDW evolutions in $RNiO_2$ and $CaCuO_2$.

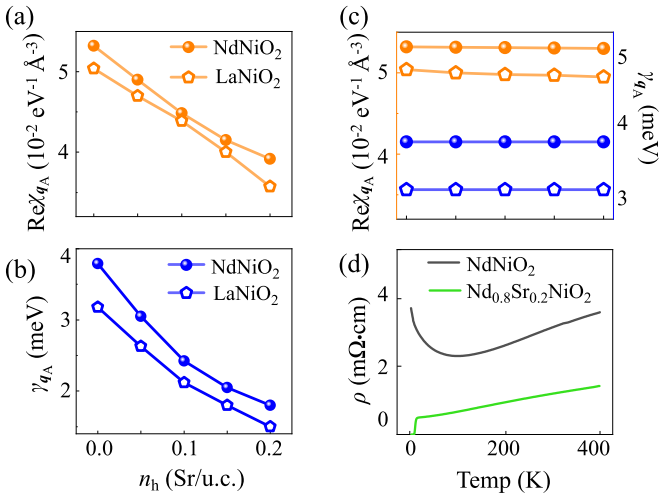

FIG. 5. Comparison of (a) static-QP $\mathrm{Re}\chi_{\boldsymbol{q}A}$ and (b) DFT-calculated $\gamma_{\boldsymbol{q}A}$ for $NdNiO_2$ and $LaNiO_2$ as functions of n_h. (c) Static-QP calculated $\mathrm{Re}\chi_{\boldsymbol{q}A}$ and DFT-calculated $\gamma_{\boldsymbol{q}A}$ as functions of temperature. (d) Experimentally measured electrical resistivity of $NdNiO_2$ (with CDW) and $Nd_{0.8}Sr_{0.2}NiO_2$ (without CDW) as functions of temperature.

The real ($\mathrm{Re}\chi$) and imaginary ($\mathrm{Im}\chi$) parts of electron susceptibility (χ) reflect the EI and FSN of a system. Note that in the original picture of ideal Peierls transition, the diverging $\mathrm{Re}\chi(\boldsymbol{q})$ at a wave vector $\boldsymbol{q}$ can trigger a $\boldsymbol{q}$-modulated CDW [55]. But in real materials, $\mathrm{Re}\chi(\boldsymbol{q})$ can never diverge but peaks at observed q_{CDW}. In the following, we focus on the discussion of $NdNiO_2$ and briefly mention the results of $LaNiO_2$ in the main text.

Figures 2(a) and 2(b) show the $\boldsymbol{q}$-dependent $\mathrm{Re}\chi(\boldsymbol{q})$ calculated using the static part of the DMFT low-energy Hamiltonian [referred to as static-QP $\mathrm{Re}\chi(\boldsymbol{q})$ hereafter] in $NdNiO_2$ along two high-symmetry lines in $q_z = 0$ and $0.5c^*$ planes as a function of n_h. The static-QP approximation is suitable because the EI is mainly driven by states near the Fermi level, where the quasiparticle states are sharp and Fermi surfaces are well defined in nickelates [44]. Overall, when $n_h = 0$, there are some similarities in these two planes, i.e., there are multiple high-intensity peaks along Γ-M (Γ-X) and Z-A (Z-R) lines appearing at similar $\boldsymbol{q}$, reflecting a quasi-2D character of band structures. Importantly, these corresponding peaks in $\mathrm{Re}\chi(\boldsymbol{q})$ are also observed in $\mathrm{Im}\chi(\boldsymbol{q})$ (Fig. 11), indicating that FSN plays important roles in forming the peaks in $\mathrm{Re}\chi(\boldsymbol{q})$. Surprisingly, with the increase of n_h, the peak intensities gradually decrease. These n_h-dependent behaviors are also observed in $LaNiO_2$ (Fig. 12). Interestingly, the n_h-dependent $\mathrm{Re}\chi(\boldsymbol{q})$ shows the opposite trend in $NdNiO_2$ and $CaCuO_2$, i.e., the peaks in $\mathrm{Re}\chi(\boldsymbol{q})$ become more noticeable under a larger n_h in $CaCuO_2$, along with the increased values of $\mathrm{Re}\chi(\boldsymbol{q})$ (Fig. 13).

To further investigate the contribution of electronic states to $\mathrm{Re}\chi(\boldsymbol{q})$ in undoped $NdNiO_2$, taking peak A as an example (other peaks are similar), the $\boldsymbol{k}$-resolved $\mathrm{Re}\chi_{\boldsymbol{q}A}(\boldsymbol{k})$ for the Ni $3d_{x2-y2}$ band (a majority contributor) is shown in Fig. 2(c), and the results for Nd $5d_{z2}$ (a minority contributor) are given in Fig. 14. Basically, for a fixed $\boldsymbol{q}$, the contributions to $\mathrm{Re}\chi$ can be divided into two parts: (i) states on FS connected by

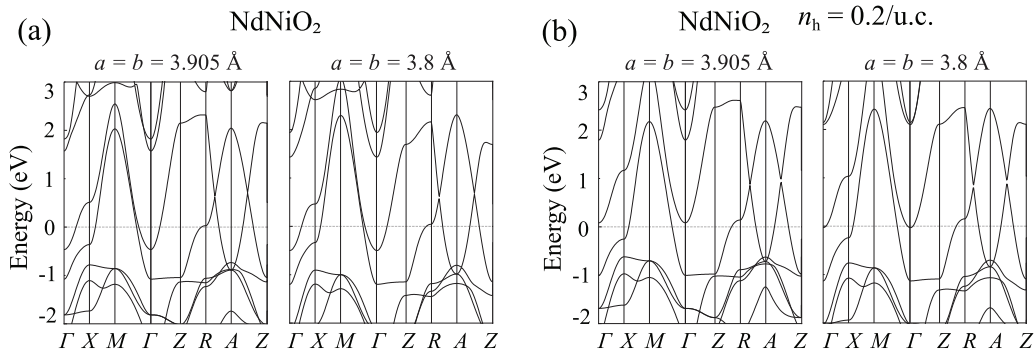

FIG. 6. DFT calculated band structures for (a) undoped and (b) Sr-doped $NdNiO_2$ under different lattice parameters. Left and right panels are for lattice parameters of $a = b = 3.905$ and 3.800 Å, respectively. (The c lattice is full relaxed.)

$\boldsymbol{q}$ [dark-blue spots in Fig. 2(c)] and (ii) occupied and unoccupied states (not on FS) connected by $\boldsymbol{q}$ [light-blue regions in Fig. 2(c)] (see Fig. 14 for more details and explanations). Importantly, while (i) strongly depends on the shape of FS and determines the peak formation to $\mathrm{Re}\chi$, (ii) is weak and mostly contributes a uniform value to $\mathrm{Re}\chi$. As shown in Fig. 2(c), the unique FS shape of $NdNiO_2$, induced by the VHS across Fermi level, makes the states on FS near the Brillouin zone (BZ) boundary well connected by $\boldsymbol{q}_A$ [red arrows in Fig. 2(c)], contributing a large value to $\mathrm{Re}\chi_{\boldsymbol{q}A}$. Importantly, the FS in the k_x-k_y plane is almost unchanged with variable k_z between $0 \leqslant k_z \leqslant 0.2c^*$ [e.g., parallel lines marked in Fig. 1(c)], and the connection vector $\boldsymbol{q}_A$ in different k_z planes keeps constant in this FS segment. The $\mathrm{Re}\chi(\boldsymbol{q})$ in different k_z planes are given in Fig. 2(d), where we can clearly see that $\mathrm{Re}\chi(\boldsymbol{q})$ all peaked at the same $\boldsymbol{q}_A$ for small k_z. Therefore, the unique parallel FS segment in undoped $NiNiO_2$ can induce a strong FSN, contributing a large peak to $\mathrm{Re}\chi(\boldsymbol{q})$.

Under hole doping, the VHS across E_F shifts to a smaller k_z value, which reduces the k_z range for parallel FS segments of the $3d_{x2-y2}$ band [i.e., the length of parallel lines marked in Fig. 1(c)], thus decreasing the strength of FSN. In addition, hole doping reduces the occupation of Nd $5d_{z2}$ states at FS, decreasing their spherelike electron pocket. Figure 2(e) shows the change of contribution from Ni $3d_{x2-y2}$ and Nd $5d_{z2}$ states to $\mathrm{Re}\chi_{\boldsymbol{q}A}$ (and other peaks) as a function of n_h. As n_h increases, the contribution of both Ni $3d_{x2-y2}$ and Nd $5d_{z2}$ decreases, explaining the observation in Fig. 2(a). Meanwhile, as the n_h increases, the evolved FS gradually shifts $\boldsymbol{q}_A$ to smaller values. On the other hand, the opposite trend of $\mathrm{Re}\chi_{\boldsymbol{q}}$ in $CaCuO_2$ under hole doping, as shown in Fig. 13, can be understood as (1) the gradual approach of VHS to Fermi level, which could increase the parallel segment of FS [Fig. 1(e)] along k_z, and (2) the lack of the $5d$ orbital. Therefore, as shown in Fig. 2(e), a n_h-dependent dome region may exist in the $\mathrm{Re}\chi_{\boldsymbol{q}\mathrm{peak}}$ of $CaCuO_2$ but not of $NdNiO_2$.

IV. ELECTRON CORRELATION EFFECT ON EI

It is interesting to compare the static-QP $\mathrm{Re}\chi(\boldsymbol{q})$ with DFT-calculated $\mathrm{Re}\chi(\boldsymbol{q})$ for both $NdNiO_2$ and $CaCuO_2$, in order to capture the partial role of electron correlation effect on $\mathrm{Re}\chi(\boldsymbol{q})$. For the case of $NdNiO_2$ (Fig. 15), the curvature shapes of $\mathrm{Re}\chi(\boldsymbol{q})$ under DMFT and DFT calculations are consistent, except for the exact peak intensities (partially due to the different sizes of the Nd $5d$ electron pocket under DFT and DMFT calculations). For the case of $CaCuO_2$ (Fig. 13), compared to $NdNiO_2$, there is stronger renormalization of $\mathrm{Re}\chi(\boldsymbol{q})$ spectra, e.g., the peaks become more noticeable under DMFT calculations than under DFT calculations under the same n_h. We speculate that the dome structure in the $\mathrm{Re}\chi_{\boldsymbol{q}\mathrm{peak}}$ of $CaCuO_2$ (obtained using DFT calculations) [Fig. 2(e)] might play some roles in the experimentally observed CDW dome structure in $CaCuO_2$-like cuprates [5,24].

In addition to our DMFT calculations for CDW-free systems, here, we also perform determinant quantum Monte Carlo (DQMC) calculations at finite temperature (below the experimentally observed CDW transition temperature) with

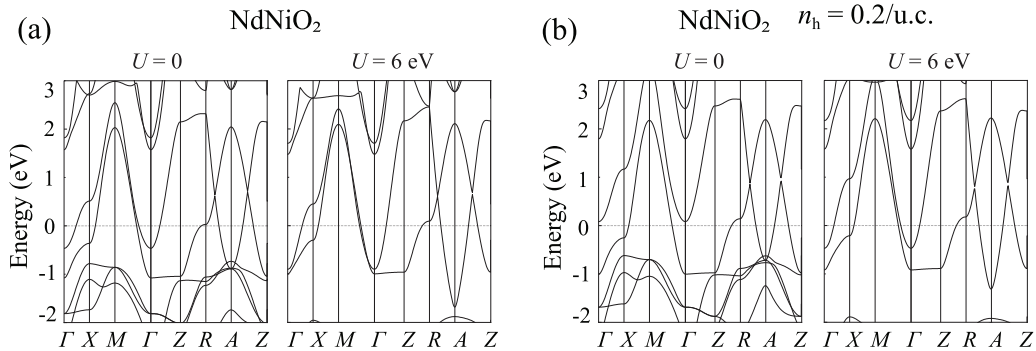

FIG. 7. DFT+U calculated band structures for (a) undoped and (b) Sr-doped $NdNiO_2$ under two largely different Hubbard U. Left and right panels are for Hubbard $U = 0$ and 6 eV, respectively.

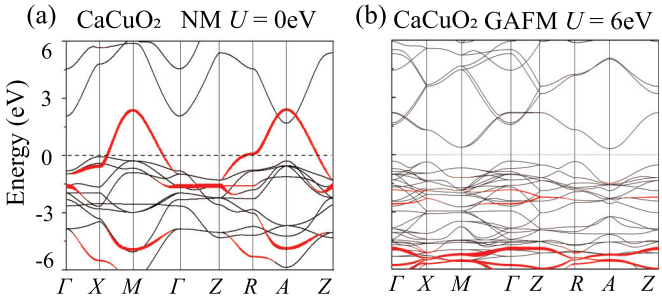

FIG. 8. DFT+U calculated band structures of $CaCuO_2$. (a) and (b) are under $U = 0$ eV (NM state) and $U = 6$ eV (G type AFM state), respectively. Red dots highlight the contributions of d_{x2-y2} orbitals in $CaCuO_2$. The ground state of parental $CaCuO_2$ is a Mott insulator.

periodic boundary conditions [56–59]. We consider a simplified two-band Hubbard model that is constructed with the major Ni $3d_{x2-y2}$ and Nd $5d_{z2}$ orbitals. Our model contains the intralayer hopping, the interlayer hopping, and the strongly correlation on the Ni layer. Importantly, the nearest-neighboring intersite Coulomb interactions are fully considered in our DQMC calculations (see Method). As shown in Figs. 19 and 20, our unbiased numerical analysis cannot develop a stripe CDW order based on the two-band Hubbard model in a 2D square lattice with periodic boundary conditions.

V. HOLE DOPING DEPENDENT MEPC

Besides the understanding of pure electron effect on CDW formation, another important issue is understanding the role of MEPC in CDW formation [60]. The MEPC can be evaluated by calculating phonon linewidth γ. Because the DFT calculations can capture basic electronic structure of $NdNiO_2$ and also because it is extremely expensive to perform MEPC under DMFT method [Fig. 1(b)], in the following we perform the MEPC calculations based on standard DFT calculations.

Figures 3(a) and 3(b) show the calculated $\boldsymbol{q}$-dependent $\gamma(\boldsymbol{q})$ in $q_z = 0$ and $0.5c^*$. Importantly, when $n_h = 0$, the $\boldsymbol{q}$ for generating high-intensity peaks in $\gamma(\boldsymbol{q})$ are generally consistent with that in $\mathrm{Re}\chi(\boldsymbol{q})$ (Fig. 15), although the relative intensities for different peaks are slightly different in these two spectra. This is an important signal that a synergetic effect exists in EI and MEPC. Remarkably, when n_h increases, the intensities of these peaks dramatically decrease, and some of them (e.g., A' and B') can even disappear at a high n_h. When n_h increases, both $\mathrm{Re}\chi(\boldsymbol{q})$ and $\gamma(\boldsymbol{q})$ are strongly weakened. The features of n_h-dependent $\gamma(\boldsymbol{q})$ are similar in $LaNiO_2$ (Fig. 21) and $NdNiO_2$. In addition, the basic features of n_h-dependent $\gamma(\boldsymbol{q})$ exist at different choices of U (Figs. 22 and 23) during the DFT calculations.

Importantly, the MEPC features in $CaCuO_2$ (Fig. 24) are quite different from that in $NdNiO_2$.

(1) In contrast to the $NdNiO_2$, the peak positions in $\gamma(\boldsymbol{q})$ are not the same as that in $\mathrm{Re}\chi(\boldsymbol{q})$ (Fig. 13), which indicate that the synergistic effect between EI and MEPC may not happen in $CaCuO_2$.

(2) The $\gamma(\boldsymbol{q})$ of $CaCuO_2$ are very insensitive to n_h, which conflicts with the experimentally observed n_h-dependent CDW formation in cuprates.

Therefore, we might conclude that, while electron effect indeed plays a dominant role in CDW formation in $CaCuO_2$-like cuprates, a joint contribution of EI and MEPC may be important for CDW formation in $NdNiO_2$.

It is important to further understand the different orbital contributions to $\gamma(\boldsymbol{q})$. Surprisingly, in contrast to $\mathrm{Re}\chi_{\boldsymbol{q}}(\boldsymbol{k})$, Nd $5d$ plays a larger role than Ni $3d$ in $\gamma(\boldsymbol{q})$. As shown in Fig. 4(a), the MEPC matrix $g(\boldsymbol{k})$ at $\boldsymbol{q}_A$ obtained from all the phonon modes highlights the major contribution of intraband scattering of Nd $5d_{z2}$. The magnitude of interband scattering between Ni $3d_{x2-y2}$ and Nd $5d_{z2}$ is similar to the intraband scattering of the Ni $3d_{x2-y2}$ orbital (Figs. 25 and 26). The DFT-calculated phonon spectrum of undoped $NdNiO_2$ is shown in Fig. 4(b). Comparing the phonon dispersion between $k_z = 0$ and $0.5c^*$ planes, it is clearly identified that there are two strongly soft optical modes around A, as indicated by the arrows. The projected $\gamma(\boldsymbol{q})$ shows that the main contribution comes from optical modes. Importantly, one soft mode partially contributes to the large $\gamma_{\boldsymbol{q}B'}$. The phonon spectrum of $LaNiO_2$ (Fig. 27) is similar to that of $NdNiO_2$. Consistently, the appearance of soft optical modes is also observed in CDW-phase $LaNiO_2$ in experiments [21]. Figure 4(c) shows the two typical strong orbital-phonon coupling modes at $\boldsymbol{q}_A$ and $\boldsymbol{q}_{B'}$, as marked in Fig. 4(b). Similar to that in cuprates [61], due to the large mass differences between Nd/Ni and O atoms, the atomic vibrations are much strong for O atoms. While the orbital components in both modes come from the Nd $5d_{z2}$ and Ni $3d_{x2-y2}$, the phonon modes can be either in-plane B_1 mode or out-of-plane A' mode. The B_1 mode contributes large EPC, and the A' mode relates to the soft phonon. We note that the complete softening of the phonon mode, which usually happens, may not be a necessary condition to form CDW, such as in cuprates (pure electron reconstruction without noticeable structure modulation) [61–64] and in $CuGeO_3$ (spin-Peierls transition in the central-peak regime) [65–67].

When n_h increases, the phonon spectrum of $NdNiO_2$ only has small changes (Fig. 27), but the occupation of Nd $5d_{z2}$ around Fermi level dramatically decreases. Consequently, as shown in Fig. 4(d), the $\gamma_{\boldsymbol{q}A}$ decreases rapidly, explaining the observation in Fig. 3. On the other hand, the lack of Ca $5d_{z2}$ around Fermi level can explain the large insensitivity of $\gamma_{\boldsymbol{q}}$ under different n_h in $CaCuO_2$ (Fig. 24).

VI. COMPARISON BETWEEN $NdNiO_2$ AND $LaNiO_2$

After understanding the EI and MEPC in $NdNiO_2$, it is interesting to compare the calculated $\mathrm{Re}\chi(\boldsymbol{q})$ and $\gamma(\boldsymbol{q})$ between $NdNiO_2$ and $LaNiO_2$. Following a similar method, we have systemically calculated the DFT and DMFT calculated $\mathrm{Re}\chi(\boldsymbol{q})$ (Fig. 12) and $\gamma(\boldsymbol{q})$ (Fig. 21). Overall, the $\mathrm{Re}\chi(\boldsymbol{q})$ and $\gamma(\boldsymbol{q})$ are similar for both systems, except for the specific values. As shown in Figs. 5(a) and 5(b), the values of $\mathrm{Re}\chi_{\boldsymbol{q}A}$ and $\gamma_{\boldsymbol{q}A}$ in $LaNiO_2$ are smaller than that of $NdNiO_2$, mostly because the occupation of La $5d_{z2}$ is smaller than that of Nd $5d_{z2}$ [Fig. 1(f)]. Under hole doping, obeying the same mechanism discussed above, the values of $\mathrm{Re}\chi_{\boldsymbol{q}A}$ and $\gamma_{\boldsymbol{q}A}$

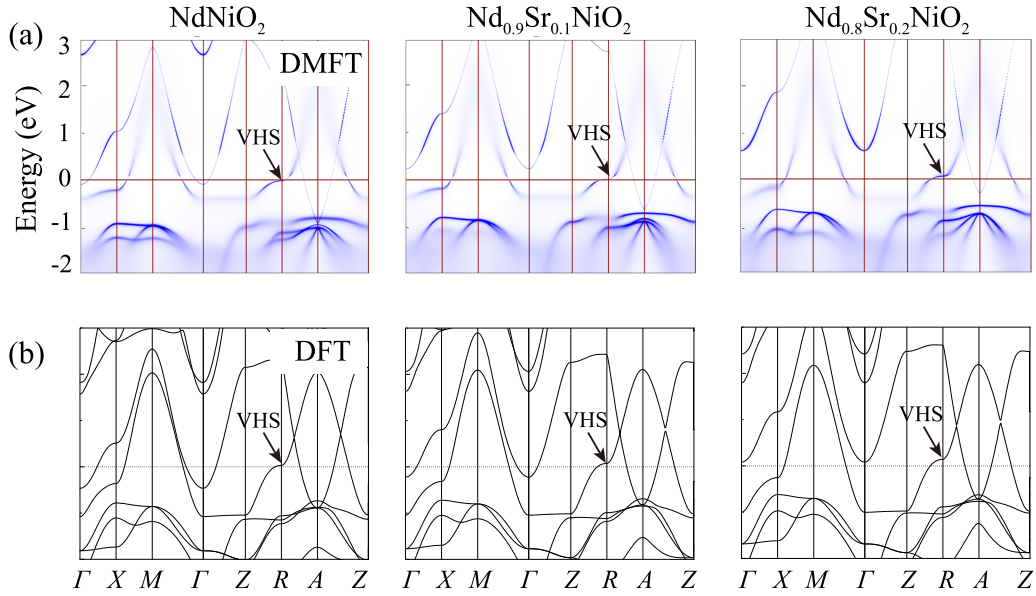

FIG. 9. (a) DMFT-calculated $\boldsymbol{k}$-resolved spectral functions and (b) DFT-calculated band structures for pristine and Sr-doped $NdNiO_2$ (in units of Sr/u.c.). Fermi level is set to zero. VHSs are labeled by arrows.

will gradually decrease in both systems, accompanied by the decreases of $\boldsymbol{q}_A$. Generally, the trends of other peaks in $\mathrm{Re}\chi_{\boldsymbol{q}}$ and $\gamma_{\boldsymbol{q}}$ and their n_h-dependent behaviors (Fig. 28) are similar to that of $\mathrm{Re}\chi_{\boldsymbol{q}A}$.

Unexpectedly, as shown in Fig. 5(c), the values of $\mathrm{Re}\chi_{\boldsymbol{q}A}$ and $\gamma_{\boldsymbol{q}A}$ are estimated to be insensitive to the electron temperature even up to 400 K for the undoped $R\mathrm{NiO}_2$ (similar for other $\boldsymbol{q}$ values, Fig. 29), indicating the strong EI and MEPC may maintain well above room temperature. Therefore, if the CDWs observed in $R\mathrm{NiO}_2$ may originate from the joint EI and MEPC, it may also survive at high temperature. In experiments, the undoped $NdNiO_2$ grown on $SrTiO_3$ substrate (without STO capping layers) may exhibit a CDW phase [22]. To confirm our theory, we perform the transport measurements using a similar CDW-phase $NdNiO_2$ sample adopted in Ref. [22]. As shown in Fig. 5(d), no signal of a sharp phase transition is observed up to 400 K in the electrical resistivity, indicating that the CDW phase in $NdNiO_2$ might survive at such a high temperature. For our $Nd_{0.8}Sr_{0.2}NiO_2$ sample with a superconducting temperature of ≈ 10 K, the CDW phase is not observed to coexist with the superconductivity using resonant inelastic x-ray-scattering measurement [22], possibly due to their competitive relationship and/or largely reduced EI and MEPC in heavy-hole-doped $R\mathrm{NiO}_2$.

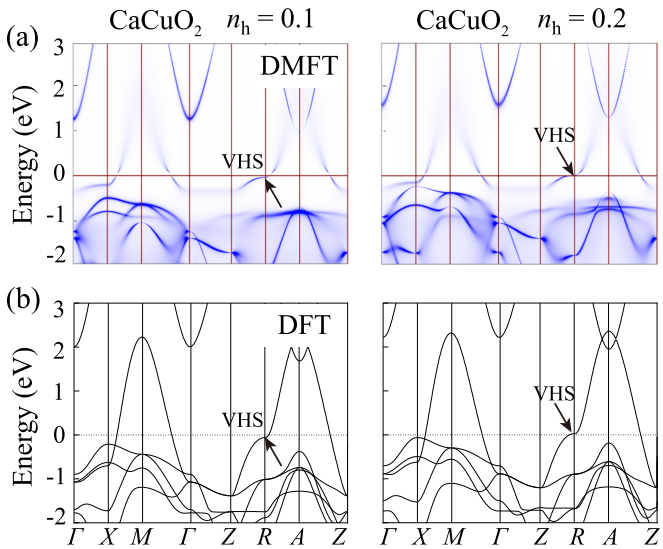

FIG. 10. (a) DMFT-calculated $\boldsymbol{k}$-resolved spectral functions and (b) DFT-calculated band structures for $0.1h$- and $0.2h$-doped $CaCuO_2$. Fermi level is set to zero. VHSs are labeled by arrows.

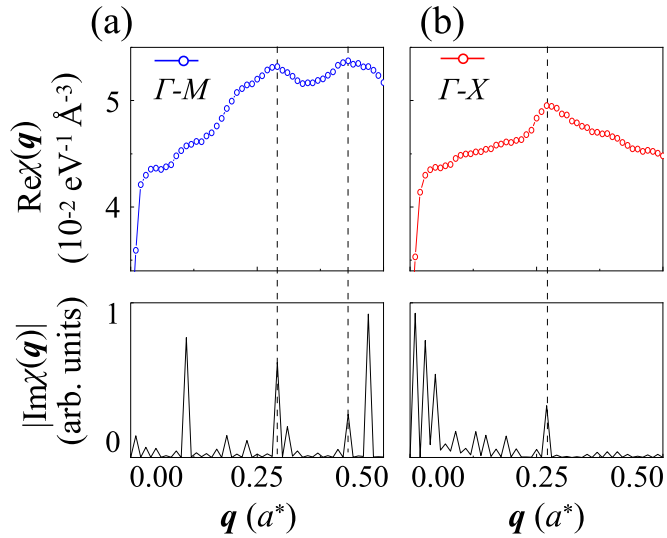

FIG. 11. DMFT static-QP calculated $\mathrm{Re}\chi(\boldsymbol{q})$ (upper panels) and $\mathrm{Im}\chi(\boldsymbol{q})$ (bottom panels) along high-symmetry lines of (a) Γ-M and (b) Γ-X in the $q_z = 0$ plane for undoped $NdNiO_2$.

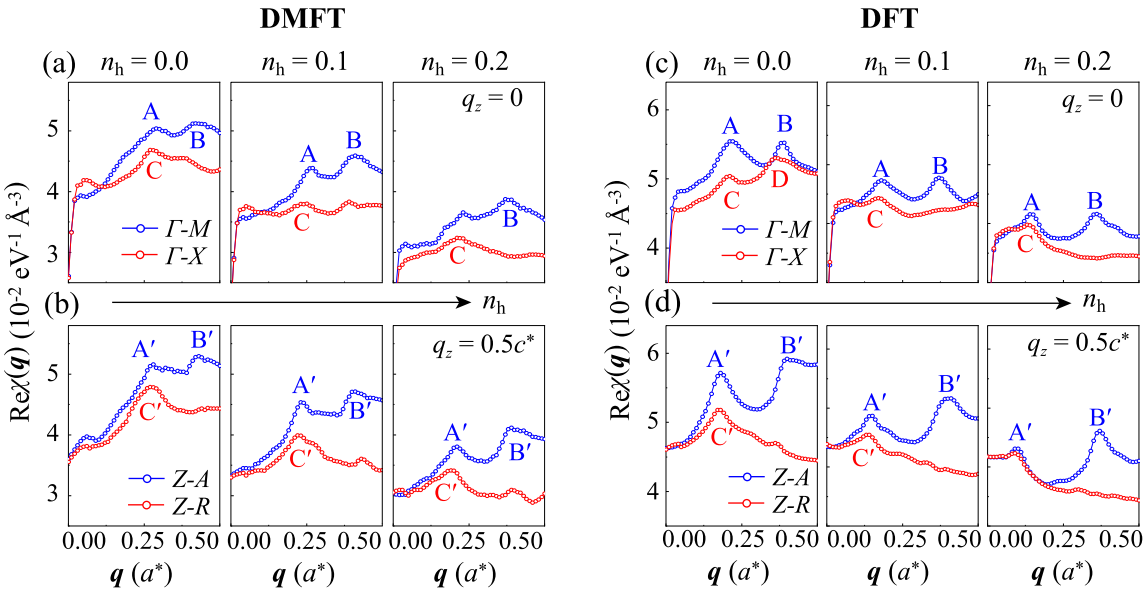

FIG. 12. (a) DMFT static-QP Re$\chi(\boldsymbol{q})$ of $LaNiO_2$ under three different n_h (in units of Sr/u.c.) along two high-symmetry lines in the $q_z = 0$ plane. (b) Same as (a) but in the $q_z = 0.5c^*$ plane. (c) and (d) are for DFT results. $A(A')$, $B(B')$, and $C(C')$ indicate the corresponding peak positions in Re$\chi(\boldsymbol{q})$ at different $\boldsymbol{q}$.

VII. COMPARISON BETWEEN THEORY AND EXPERIMENTAL OBSERVATIONS

It is important to compare our theory with the existing experimental observations. First, it is observed in experiments that the R $5d_{z^2}$ and Ni $3d_{x2-y2}$ orbitals are resonant during the formation of CDWs in RNiO$_2$ [22], consistent with our theoretical calculations. More importantly, beyond the experimental observations, our theory further reveals that the Ni $3d_{x2-y2}$ and R $5d_{z^2}$ play the major role in forming strong EI and MEPC in undoped RNiO$_2$, respectively, which may in turn result in a very high-temperature CDW phase (at least) up to 400 K. In comparison, the CDWs observed in many cuprates are typically below $\approx$ 250 K [4,5]. Meanwhile, the superconducting T_c of nickelates (10–20 K) [8,9] are substantially one order of magnitude lower than those of cuprates (100–200 K) [1,2]. If we assume the CDW origins in nickelates and cuprates are similar, it is natural to expect that the CDW temperatures in both systems are similar, or at least are of similar order to superconducting T_c if both are originating from electronic interactions. Therefore, these facts indicate the CDW origin in nickelates and cuprates may be different. We suggest that a joint EI and MEPC is required to induce the CDW in nickelates, while EI driven by strong correlation may be the major reason for CDW formation in cuprates. In a recent work, it is revealed that the MEPC can be further enhanced by electron correlation effect [68].

Second, it is observed in experiments that hole doping gradually destabilizes or even suppresses the CDW phase in RNiO$_2$ [21,22], which is strongly different from (even opposite to) that in cuprates [4]. It may also be explained by our theory. Especially, our theory demonstrates that as n_h increases, the shift of VHS and the rapid decrease of the R $5d_{z^2}$ orbital at FS largely weaken EI and MEPC in RNiO$_2$.

Finally, it is important but still challenging to identify the exact $\boldsymbol{q}_{\rm CDW}$, because not only the 3D structure of CDW but also the out-of-plane vector of $\boldsymbol{q}_{\rm CDW}$ cannot be accurately clarified in the experiments. And we cannot decide which peak dominates the response in the real experiment, as there may be many possible factors, and further studies are needed.

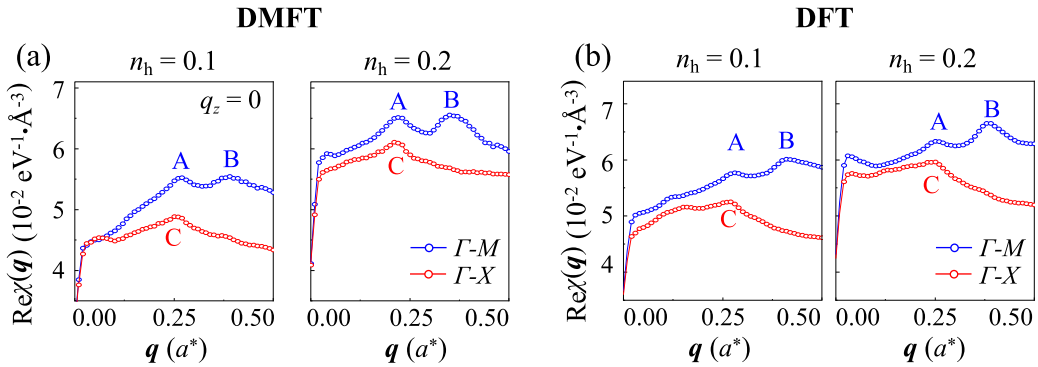

FIG. 13. (a) DMFT static-QP Re$\chi(\boldsymbol{q})$ of $CaCuO_2$ under different n_h (in units of hole/u.c.) along two high-symmetry lines in the $q_z = 0$ plane. (b) DFT results. $A(A')$, $B(B')$, and $C(C')$ indicate the corresponding peak positions in Re$\chi(\boldsymbol{q})$ at different $\boldsymbol{q}$.

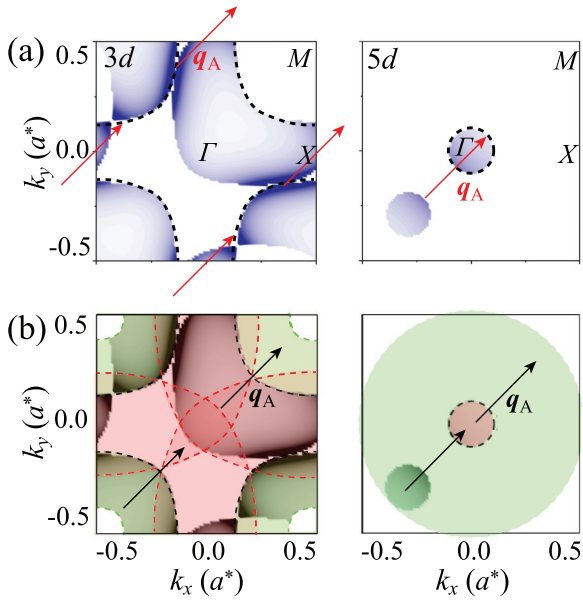

FIG. 14. (a) $\boldsymbol{k}$-resolved $\mathrm{Re}\chi_{\boldsymbol{q}}(\boldsymbol{k})$ in the $k_z = 0$ plane with $\boldsymbol{q} = \boldsymbol{q}_A$ for undoped $NdNiO_2$, which is projected to the Ni $3d_{x2-y2}$ orbital (left panel) and the Nd $5d_{z2}$ orbital (right panel). Black-dashed lines represent the FS of these two bands and red arrows of $\boldsymbol{q}_A$ connect the electronic states on the FS (dark-blue spots) to form a nesting (in view of almost unchanged FS along k_z). (b) Illustration of the contribution to $\mathrm{Re}\chi_{\boldsymbol{q}_A}(\boldsymbol{k})$ from occupied and unoccupied states connected by $\boldsymbol{q}_A$ for the Ni $3d_{x2-y2}$ band (left panel) and the Nd $5d_{z2}$ band (right panel). Only the occupied states in the red-shaded region and unoccupied states in the green-shaded region, that can be connected to each other by $\boldsymbol{q}_A$ (black arrow), contribute to $\mathrm{Re}\chi_{\boldsymbol{q}_A}(\boldsymbol{k})$ [light-blue regions in (a)].

However, by assuming a specific q_z, we can clearly identify the peaks at (0.333, 0) in $NdNiO_2$ and at (0.344, 0) in $LaNiO_2$ in both $\mathrm{Re}\chi(\boldsymbol{q})$ and $\gamma(\boldsymbol{q})$ spectra, which may trigger the experimentally observed CDW with $\boldsymbol{q}_{\mathrm{CDW}}$ at (0.333, 0) in $NdNiO_2$ and at (0.344, 0) in $LaNiO_2$ (Fig. 30), respectively. Again, our calculations not only indicate that a joint EI and MEPC is important for CDW formation in nickelates, but also predict that the $\boldsymbol{q}_{\mathrm{CDW}}$ in $LaNdO_2$ and $NdNiO_2$ could be very similar due to their nearly identical peaks in $\mathrm{Re}\chi(\boldsymbol{q})$ and $\gamma(\boldsymbol{q})$, consistent with the experimental observations [21,22]. In practice, the exact $\boldsymbol{q}_{\mathrm{CDW}}$ may also highly depend on the local environments, point and external defects [69], and structural disorders [21,70], which deserves to be clarified in the future. Since the understanding of CDW in nickelates is at the very beginning, further studies are needed to confirm its origin.

VIII. METHODS

A. DFT calculations

The crystal structure optimizations are performed using DFT calculations as implemented in Quantum ESPRESSO (QE) [71], and the scalar relativistic ultrasoft pseudopotentials are used [72]. The kinetic energy cutoff for plane waves is set to 80 Ry. Some calculations are also tested using the Vienna *ab initio* simulation package [73] within the projector augmented wave method [74] and Perdew-Burke-Ernzerhof [75] exchange correlation functional, which give the same results as QE. The lattice constants in the xy plane are fixed at $a = b = 3.905$ Å to match the $SrTiO_3$ substrate, while the lattice in the z direction is fully relaxed, which gives $c = 3.34$ and 3.45 Å for $NdNiO_2$ and $LaNiO_2$. The van der Waals correction is adopted [76]. The EPC calculations are performed by Wannier interpolation [77,78], as implemented in the EPW code [79], which allows us to achieve sufficiently accurate k-point sampling in the BZ. The on-site Hubbard U [80,81] is also considered, which is added on the $3d$ orbitals of Ni. The temperature effect is considered as implemented in the Fermi-Dirac distribution. To simulate the real Sr-induced hole doping effect, the virtual crystal approximation [82] is achieved by replacing a fraction of R with Sr. Note that electron correlation effects are not taken into account in phonon calculations.

B. DMFT calculations

The many-body calculations are done by DFT+DMFT method using EDMFT embedded in the WIEN2K package [83]. Because the valence of Nd atoms is very close to 3^+, whose f electrons are localized and do not hybridize with the conduction electron, we treat Nd f electrons as the core level. The on-site Coulomb interaction for Ni $3d$ is chosen to be $U = 6.0$ eV and $J = 0.9$ eV, as a very recent experimental measurement indicates that $U \approx 5$ eV is very suitable for $RNiO_2$ [84,85]. The local impurity problem is solved using continuous-time quantum Monte Carlo (QMC) method [86] at 116 K ($\beta = 100\,\mathrm{eV}^{-1}$), with 2×10^9 QMC steps for each DMFT iteration. For the nickelates, the nominal double-counting scheme with $n_f = 9.0$ was employed, while for the cuprate, the double counting energy was fixed at $E_{\mathrm{DC}} =$ 71.3 eV to ensure d^9 occupation for the pristine compound.

The low-energy Hamiltonian in DMFT calculation was obtained by projecting the states within [–10.0, 10.0] eV with respect to the Fermi level, which contains 25 states, including Ni $3d$, O $2p$, Nd $5d$, and some other higher-energy states (for $CaCuO_2$, it contains 16 states, including Cu-$3d$, O-$2p$, and Ca-$3d$). The model Hamiltonian reads

$$H = H_{\mathrm{LDA}} - H_{\mathrm{dc}} + H_{\mathrm{int}} \tag{1}$$

where

$$H_{\mathrm{LDA}} = \sum_{im,jm',\sigma} (\varepsilon_{im}\delta_{im,jm'} + t_{im,jm'}) c^{\dagger}_{im\sigma} c_{jm'\sigma} \tag{2}$$

is the DFT Hamiltonian, where i and j are atomic site indices, m and m' are orbital indices, and σ labels spins. H_{int} contains the full Coulomb interactions within the Ni-$3d$ (Cu-$3d$) orbitals' subspace. H_{DC} is the double-counting term. Vertex correction, which may be important for understanding the origin of CDW formation in nickelate systems, is not considered in our current paper

C. Electron susceptibility $\chi(q)$ and phonon linewidth $\gamma(q)$

The real $\mathrm{Re}\chi(\boldsymbol{q})$ and imaginary $\mathrm{Im}\chi(\boldsymbol{q})$ parts of electron susceptibility [87] are calculated by

$$\begin{aligned} \mathrm{Re}\chi(\boldsymbol{q}) &= \sum_{\boldsymbol{k}} \frac{f(\varepsilon_{\boldsymbol{k}}) - f(\varepsilon_{\boldsymbol{k}+\boldsymbol{q}})}{\varepsilon_{\boldsymbol{k}} - \varepsilon_{\boldsymbol{k}+\boldsymbol{q}}}, \\ \mathrm{Im}\chi(\boldsymbol{q}) &= \sum_{\boldsymbol{k}} \delta(\varepsilon_{\boldsymbol{k}} - \varepsilon_F)\delta(\varepsilon_{\boldsymbol{k}+\boldsymbol{q}} - \varepsilon_F), \end{aligned} \tag{3}$$

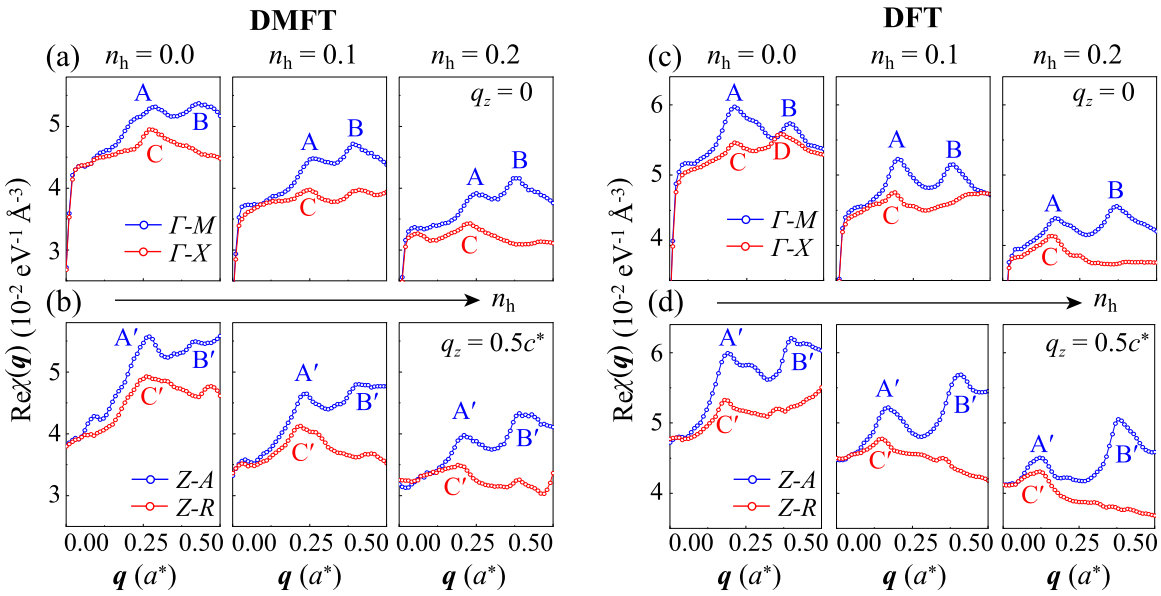

FIG. 15. DMFT static-QP Re$\chi(\boldsymbol{q})$ for $NdNiO_2$ under three different n_h (in units of Sr/u.c.) along two high-symmetry lines in (a) the $q_z = 0$ plane and (b) the $q_z = 0.5c^*$ plane using DMFT method. (c) and (d) are the same as (a) and (b) but for DFT calculations. $A(A')$, $B(B')$, $C(C')$, and D indicate the major corresponding peak positions in Re$\chi(\boldsymbol{q})$ at different $\boldsymbol{q}$.

Where $f(\varepsilon_{\boldsymbol{k}})$ is the function of the Fermi-Dirac distribution. The real part reflects the stability of the electronic system, and the imaginary part reflects the Fermi surface topology of a system. The phonon linewidth $\gamma(\boldsymbol{q})$ which directly reflects the electron-phonon coupling strength is defined as

$$\gamma(\boldsymbol{q}, \nu) = 2\pi\omega_{\boldsymbol{q}\nu} \sum_{mn} \int \frac{d\boldsymbol{k}}{\Omega_{\mathrm{BZ}}} |g_{mn,\boldsymbol{q}\nu}(\boldsymbol{k})|^2 \times \delta(\varepsilon_{m,\boldsymbol{k}} - \varepsilon_F)\delta(\varepsilon_{n,\boldsymbol{k}+\boldsymbol{q}} - \varepsilon_F), \quad (4)$$

where m and n are the band indices, and ν represents the phonon mode. The coupling matrix is

$$g_{mn,\boldsymbol{q}\nu}(\boldsymbol{k}) = \frac{1}{\sqrt{2\omega_{\boldsymbol{q}\nu}}} \langle \varphi_{m,\boldsymbol{k}} | \partial_{\boldsymbol{q}\nu} V | \varphi_{n,\boldsymbol{k}+\boldsymbol{q}} \rangle, \quad (5)$$

where $\varphi_{m,\boldsymbol{k}}$ is the electronic wave function, with eigenvalue $\varepsilon_{m,\boldsymbol{k}}$.

The static part of the DMFT low-energy Hamiltonian is used to calculate the bare-electron susceptibility, and the temperature dependence contains only the smearing of the Fermi surface.

D. QMC calculations

The DQMC calculations are performed at finite temperature (below the experimentally observed CDW transition temperature) with periodic boundary conditions [57–60]. The partition function in DQMC is expressed as a high-dimensional integral on a set of random auxiliary fields which can be done by the Monte Carlo simulations. We use 30 000 sweeps to reach equilibrium and 80 000 sweeps further to take the measurements. Two square sublattices are used with a scale of $L = 14$ (the total number of lattice sites is $N_s = 2 \times L^2 = 392$). Here, a two-band effective model is constructed containing Ni $3d_{x2-y2}$ and Nd $5d_{z2}$ orbitals [14,47]. The two-band Hubbard model employed contains the intralayer hopping, the interlayer hopping, and the strongly correlated Ni layer [88–91].

E. Experimental methods

The $NdNiO_2$ films with infinite-layer structure are prepared by topochemical reduction of perovskite $NdNiO_3$ without capping layer. $NdNiO_3$ films (thickness about 10 nm) are deposited on TiO_2-terminated STO (001) substrates by a 248-nm KrF laser. During the deposition, the substrate temperature is controlled at 620 °C with the oxygen pressure of 200 mTorr. A laser fluence of 1.2 J/cm^2 is used to ablate the target and the size of the laser spot is about 3 mm^2. After deposition, the samples are cooled down in the same oxygen pressure at the rate of 10 °C/ min. In order to acquire the infinite-layer nickelate phase, the as-grown samples are sealed in the quartz tube together with 0.1 g CaH_2. The pressure of the tube is about 0.3 mTorr. Then, the tube is heated up to 290 °C in the tube furnace and held for 2 h and cooled down naturally with the ramp rate of 10 °C/ min. The superconducting $Nd_{0.8}Sr_{0.2}NiO_2$ films are prepared in the same way as the parent $NdNiO_2$. The crystal structures of films are characterized using a Bruker D8 Discover diffractometer. The temperature-dependent resistivity is measured using four-probe method in a physical properties measurement system (Quantum Design).

ACKNOWLEDGMENTS

We thank Dr. J. G. Guo at Institute of Physics (IOP) for the help on the measurements of electrical resistivity of $NdNiO_2$ and $Nd_{0.8}Sr_{0.2}NiO_2$ at different temperatures and Dr. Z. Liu at Tsinghua University for the valuable comments on our results. We acknowledge the

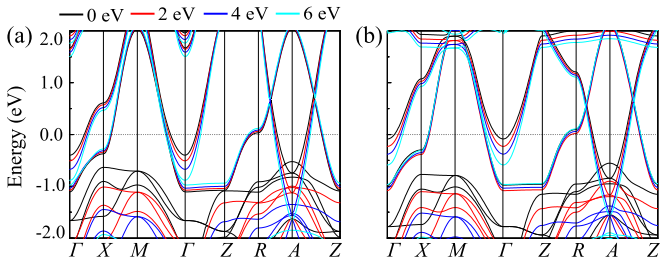

FIG. 16. Band structures of undoped (a) $NdNiO_2$ and (b) $LaNiO_2$ with different U. Black, red, blue, and cyan lines represent the electronic bands for U values of 0, 2, 4, and 6 eV, respectively.

support from the National Natural Science Foundation of China (Grants No. 11874138, No. 12004030, and No. 12088101) and the NSAF (Grant No. U2230402). The calculations were performed at Tianhe2-JK at Beijing Computational Science Research Center (CSRC).

X.S. and J.W. contributed equally to this paper.

APPENDIX

1. Hole doping dependent band structures and Fermi surfaces for $NdNiO_2$ and $CaCuO_2$

As shown in Figs. 6 and 7, the different structure parameters and Coulomb repulsion U have limited impact on the position of VHS for either parent or doping $NdNiO_2$. In the main text, the in-plane lattice constant of $RNiO_2$ is fixed to 3.905 Å, which is the lattice constant of the STO substrate. Figure 8 gives the band structures of $CaCuO_2$ with projected d_{x2-y2} orbitals.

For the case of $NdNiO_2$ [Fig. 9(a)], interestingly, we observe that the Sr doping gives rise to nonrigid shift of different orbitals, i.e., the electron pocket at the Γ point (induced by the Nd $5d$ orbital) is quickly suppressed while the electron pocket at the A point (induced by an interstitial s-like orbital) upshifts moderately, in agreement with the DFT results [Fig. 9(b)]. The Ni $3d_{x2-y2}$, the most correlated orbital, shifts upwards slightly upon Sr doping. For the case of $CaCuO_2$ (Fig. 10), there is only one single Cu $3d_{x2-y2}$ band across the Fermi level, which shifts upwards slightly upon hole doping.

2. Calculated $\mathrm{Re}\chi(\boldsymbol{q})$ and $\mathrm{Im}\chi(\boldsymbol{q})$ of $NdNiO_2$, $LaNiO_2$, and $CaCuO_2$

In the current paper, we calculate electron susceptibility $\chi(\boldsymbol{q})$ using the static part of the DMFT low-energy Hamiltonian, i.e., $H_0 + \Sigma(\omega = 0)$. We believe that it is a good approximation to the DMFT susceptibility without vertex correction: $\chi_{q(\upsilon)} = \sum_{\boldsymbol{k}} G(\boldsymbol{k}, i\omega)\, G(\boldsymbol{k}+\boldsymbol{q}, \upsilon + i\omega)$ in the current studied systems. This is because the electron instabilities are mainly driven by states near the Fermi level, and that the quasiparticle states are sharp and Fermi surfaces are well defined in the current studied systems.

As shown in Fig. 11, for two high-symmetry lines, the corresponding peaks in $\mathrm{Re}\chi(\boldsymbol{q})$ are also observed in $\mathrm{Im}\chi(\boldsymbol{q})$, indicating that FSN plays important roles in forming the peaks in the $\mathrm{Re}\chi(\boldsymbol{q})$.

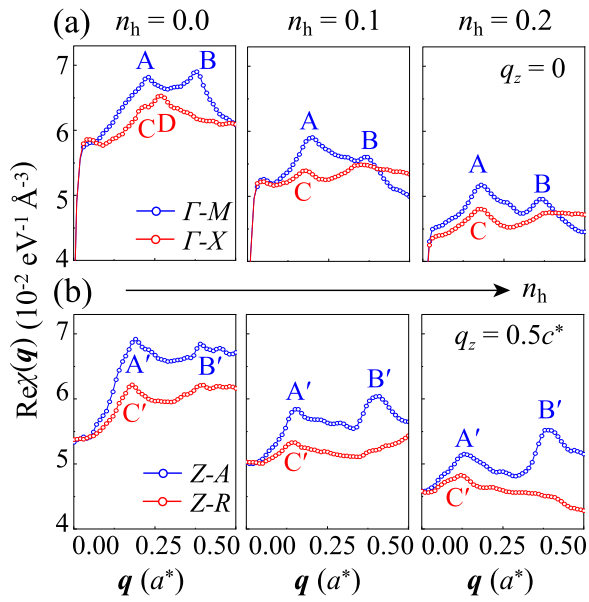

FIG. 17. (a) DFT-calculated $\mathrm{Re}\chi(\boldsymbol{q})$ of $NdNiO_2$ under three different n_h (in units of hole/u.c.) along two high-symmetry lines in the $q_z = 0$ plane with $U = 6$ eV. (b) Same as (a) but in the $q_z = 0.5c^*$ plane.

Figure 12 gives the $\mathrm{Re}\chi(\boldsymbol{q})$ for the high-symmetry lines in $q_z = 0$ (upper panel) and $q_z = 0.5c^*$ (bottom panel) planes of $LaNiO_2$. Apparently, both values of $\mathrm{Re}\chi(\boldsymbol{q})$ are slightly smaller than those of $NdNiO_2$. Upon doping, the peak intensities reduce sharply with the shift of peak positions, similar to the situation observed in $NdNiO_2$. More strikingly, the wave vectors $\boldsymbol{q}$ at the maximum are also very identical to that of $NdNiO_2$, not only in the parent phase but even in the hole doping case [$\boldsymbol{q}_A = (0.29a^*, 0.29b^*, 0)$ and $\boldsymbol{q}_B = (0.43a^*, 0.43b^*, 0)$ along Γ-M, $\boldsymbol{q}_C = (0.27a^*, 0, 0)$ along Γ-X, $\boldsymbol{q}_{A'} = (0.27a^*, 0.27b^*, 0.50c^*)$ and $\boldsymbol{q}_{B'} = (0.42a^*, 0.42b^*, 0.50c^*)$

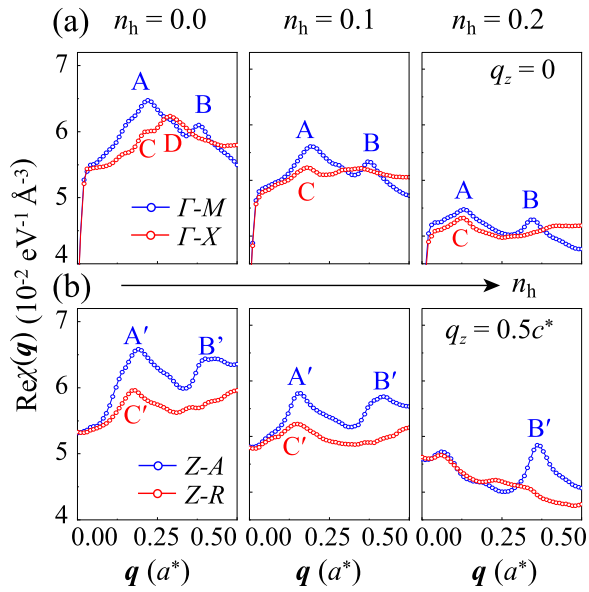

FIG. 18. Same as Fig. 17 but for $LaNiO_2$.

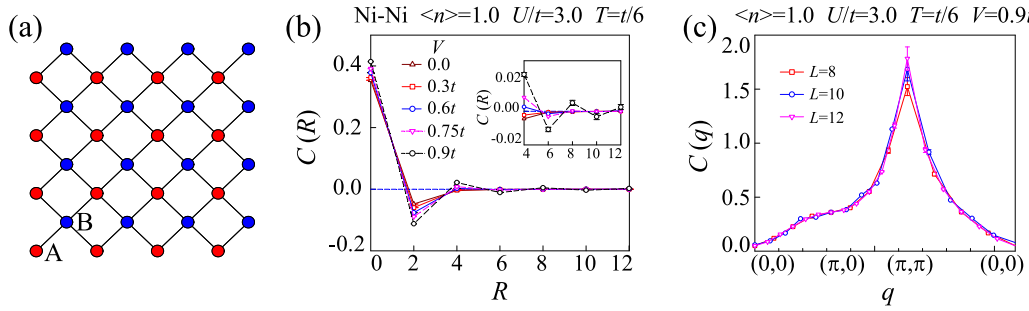

FIG. 19. (a) Lattice diagram used in the two-band Hubbard model. Red and blue circles represent sublattices A and B, corresponding to Nd $5d$ and Ni $3d$ orbitals. (b) Density-density correlations $C(R)$ of the Ni $3d$ orbital as a function of distance R (horizontal or vertical direction of the lattice) for different V at half filling $\langle n\rangle = 1.0$ and temperature $T = t/6$. Inset: The enlarged $C(R)$ for $R \geqslant 4.0$. (c) The density-density correlations $C(q)$ at $\langle n\rangle = 1.0$, $U/t = 3.0$, and $T = t/6$ on a $2 \times L2$ lattice.

along Z-A, and $\boldsymbol{q}_{C'} = (0.26a^*, 0, 0.50c^*)$ along Z-R for parent phases]. Interestingly, the n_h-dependent $\mathrm{Re}\chi(\boldsymbol{q})$ shows opposite trend in $CaCuO_2$, i.e., the peaks in $\mathrm{Re}\chi(\boldsymbol{q})$ become more noticeable under a larger n_h in $CaCuO_2$, along with the increased values of $\mathrm{Re}\chi(\boldsymbol{q})$ (Fig. 13).

To further investigate the contribution of electronic states to $\mathrm{Re}\chi(\boldsymbol{q})$ in $NdNiO_2$, taking peak A in the $k_z = 0$ plane as an example, the $\boldsymbol{k}$-resolved $\mathrm{Re}\chi_{\boldsymbol{q}A}(\boldsymbol{k})$ for Ni $3d_{x2-y2}$ and Nd $5d_{z2}$ are given in Fig. 14(a). Obviously, the contribution of Ni $3d_{x2-y2}$ (left panel) is significantly larger than that of Nd $5d_{z2}$ (right panel). Basically, for a fixed $\boldsymbol{q}$, the contributions to $\mathrm{Re}\chi$ can be divided into two parts: (i) states on FS connected by $\boldsymbol{q}$ [dark-blue spots in Fig. 14(a)] and (ii) occupied and unoccupied states (not on FS) connected by $\boldsymbol{q}$ [light-blue regions in Fig. 14(a)]. Importantly, while (i) strongly depends on the shape of FS and determines the peak formation to $\mathrm{Re}\chi$, (ii) is weak and only contributes a uniform value to $\mathrm{Re}\chi$. As shown in Fig. 14(a), the unique FS shape of $NdNiO_2$ makes the states on FS near the BZ boundary well connected by $\boldsymbol{q}_A$ [red arrows in Fig. 14(a)], contributing a large value to $\mathrm{Re}\chi_{\boldsymbol{q}A}$. As discussed in the main text [Fig. 2(a)], since the FS in the k_x-k_y plane is almost unchanged with varying k_z between $0 \leqslant k_z \leqslant 0.2c^*$, the connection vector $\boldsymbol{q}_A$ in different k_z planes keeps constant in this range. In addition, electronic states not on FS also make contributions to $\mathrm{Re}\chi_{\boldsymbol{q}A}(\boldsymbol{k})$. As shown in Fig. 14(b), only the occupied states in the red-shaded region and unoccupied states in the green-shaded region, that can be connected to each other by $\boldsymbol{q}_A$ (black arrow) around E_F, contribute to a small value of $\mathrm{Re}\chi_{\boldsymbol{q}A}(\boldsymbol{k})$ [light-blue regions in Fig. 14(a)]. Again, the electronic states contributed from Ni $3d_{x2-y2}$ [left panel, Fig. 14(b)] are larger than that of Nd $5d_{z2}$ [right panel, Fig. 14(b)].

3. Electron correlation effect on EI

It is interesting to compare the DMFT static-QP $\mathrm{Re}\chi(\boldsymbol{q})$ with DFT-calculated $\mathrm{Re}\chi(\boldsymbol{q})$ for both $NdNiO_2$ and $CaCuO_2$, in order to capture the role of electron correlation effect on $\mathrm{Re}\chi(\boldsymbol{q})$. For the case of $NdNiO_2$ (Fig. 15), the curvature shapes of $\mathrm{Re}\chi(\boldsymbol{q})$ under DMFT and DFT calculations are consistent, except for the exact peak intensities (partially due to the different sizes of the Nd $5d$ electron pocket under DFT and DMFT calculations). For the case of $CaCuO_2$ (Fig. 13), compared to $NdNiO_2$, there is stronger renormalization of $\mathrm{Re}\chi(\boldsymbol{q})$ spectra, e.g., the peaks become more noticeable under DMFT calculations than under DFT calculations under

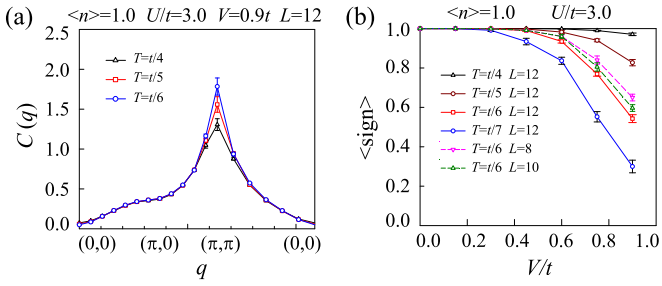

FIG. 20. (a) The density-density correlations $C(q)$ at $\langle n\rangle = 1.0$ and $V = 0.9t$ on a 2×122 lattice for different T. (b) Average sign <sign> as a function of nearest-neighbor interaction V for different temperatures at $\langle n\rangle = 1.0$, $U/t = 3.0$, and $k_z = 0$ on a 2×122 or 2×82 lattice.

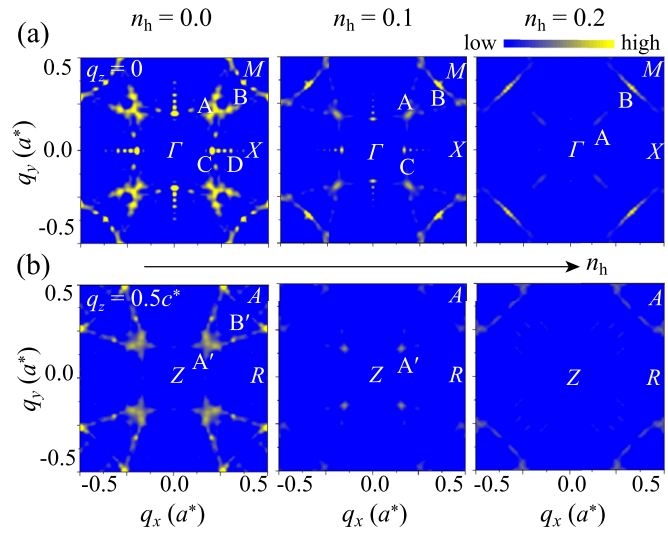

FIG. 21. (a) DFT-calculated $\boldsymbol{q}$-resolved $\gamma(\boldsymbol{q})$ under three different n_h (in units of Sr/u.c.) in the $q_z = 0$ plane from all phonon modes for electronic states in the entire BZ for $LaNiO_2$. (b) Same as (a) but in the $q_z = 0.5c^*$ plane. $A(A')$, $B(B')$, and $C(C')$ indicate the corresponding peak positions in $\gamma(\boldsymbol{q})$ at different $\boldsymbol{q}$, consistent with those in $\mathrm{Re}\chi(\boldsymbol{q})$.

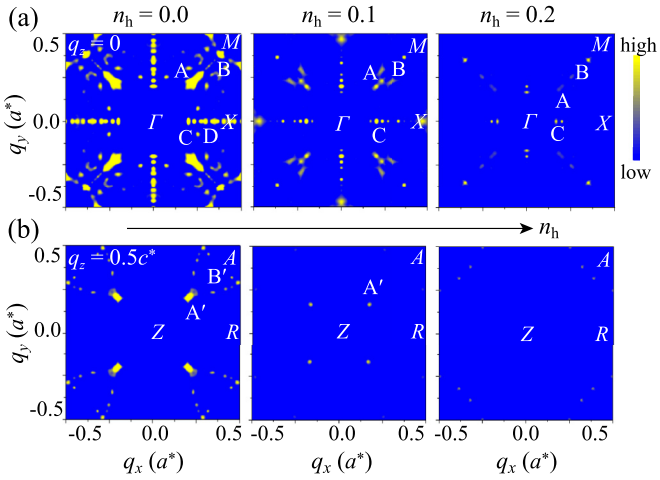

FIG. 22. (a) Calculated $\gamma(\boldsymbol{q})$ of $NdNiO_2$ from all the phonon modes in the entire BZ in the $q_z = 0$ plane with $U = 6$ eV. (b) Same as (a) but in the $q_z = 0.5c^*$ plane.

the same n_h, which is partially due to the stronger electron correlation induced larger band renormalization in $CaCuO_2$ than in $NdNiO_2$.

A comparison of DFT band structures with consideration of on-site Hubbard U is given in Fig. 16. For both $NdNiO_2$ and $LaNiO_2$ around E_F, with increasing U, the band dominated by the Nd/La $5d_{z^2}$ orbital shifts downwards significantly, making the electron pocket around the Γ point larger, while the band dominated by Ni $3d_{x^2-y^2}$ shifts upwards slightly. Importantly, with a fixed U, the occupation of La $5d_{z^2}$ [Fig. 16(b)] is always smaller than that of Nd $5d_{z^2}$ [Fig. 16(a)].

DFT-calculated $\mathrm{Re}\chi(\boldsymbol{q})$ with $U = 6$ eV for $NdNiO_2$ and $LaNiO_2$ are shown in Figs. 17 and 18, respectively. All the results of electron susceptibility with $U = 6$ eV are very similar to those with $U = 0$ eV (Figs. 12 and 15). Besides, the peak values for both $\mathrm{Re}\chi(\boldsymbol{q})$ are even larger than those with $U = 0$ eV, indicating a stronger EI. Therefore, the consideration of U could even strengthen our major DFT conclusion in the main text.

It is interesting to check the role of pure electron correlation effect on the CDW formation in nickelates, in addition

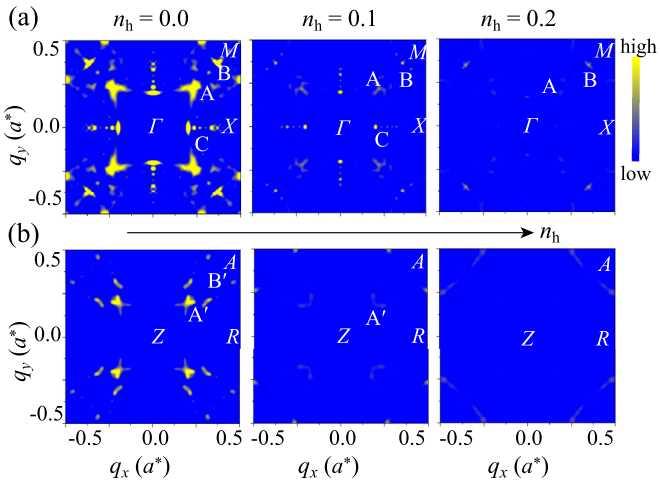

FIG. 23. Same as Fig. 22 but for $LaNiO_2$.

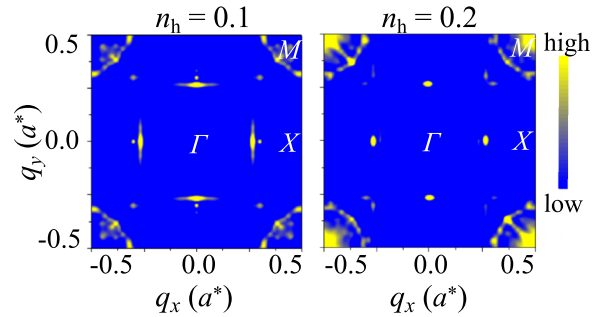

FIG. 24. Calculated $\gamma(\boldsymbol{q})$ of $CaCuO_2$ from all the phonon modes in the entire BZ in the $q_z = 0$ plane with $U = 6$ eV.

to our DMFT calculations for CDW-free systems. Here, we perform DQMC calculations at finite temperature (below the experimentally observed CDW transition temperature) with periodic boundary conditions to evaluate the electronic correlations in CDW. The partition function in DQMC is expressed as a high-dimensional integral on a set of random auxiliary field which can be done by the Monte Carlo simulations. We used 30 000 sweeps to reach equilibrium and 80 000 sweeps further to take the measurements. Two square sublattices are used with scale of $L = 12$ [see Fig. 19(a) (the total number of lattice sites is $N_s = 2 \times L^2 = 288$)]. Here, a two-band effective model is constructed containing Ni $3d_{x2-y2}$ and Nd $5d_{z2}$ orbitals. The reason that we choose Nd-$5d_{z2}$ and not the Nd$-5d_{xy}$ orbital is as follows.

(1) The two-orbital model of Ni$-5d_{z2}$ and Ni$-3d_{x2-y2}$ can well reproduce the first-principles band structure of $NdNiO_2$ which is adopted to construct the microscopic Hamiltonian in previous work [47].

(2) The onsite energy of Ni$-5d_{z2}$ is closer to Fermi level which is 0.50 eV lower than that of Nd$-5d_{xy}$.

(3) The orbital projection of Nd-d_{xy} at the A pocket is actually small, much smaller than that of Ni-$5d_{z2}$ at the Γ pocket.

The two-band Hubbard model employed contains the intralayer hopping, the interlayer hopping, and the strongly correlated Ni layer, which can be written as

$$H = H_1 + H_2 + H_3 + H_4 + H_5,$$

$$H_1 = t_3^{\mathrm{Nd-Ni}} \sum_{i\eta\sigma} [a_{i\sigma}^{\dagger} b_{i+\eta\sigma} + \mathrm{H.c.}],$$

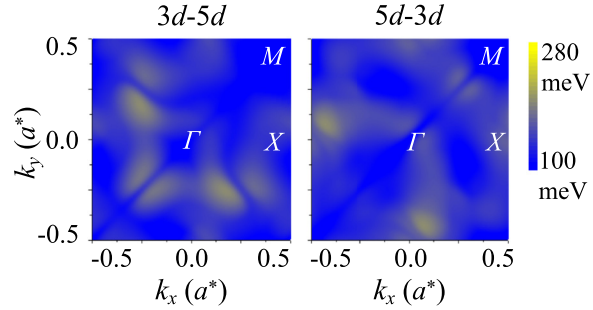

FIG. 25. Interband coupling matrix g($\boldsymbol{k}$) between Ni $3d_{x2-y2}$ and Nd $5d_{z^2}$ orbitals in $NdNiO_2$ for $\boldsymbol{q}_A = (0.22a^*,\ 0.22b^*,\ 0)$ in the $k_z = 0$ plane.

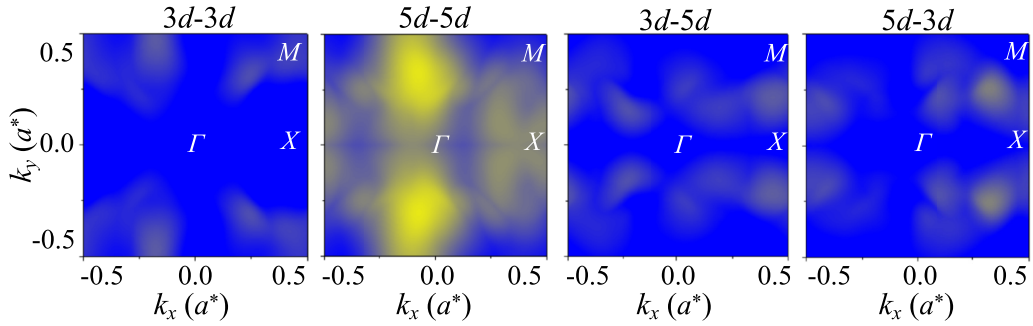

FIG. 26. Band- and $\boldsymbol{k}$-resolved g($\boldsymbol{k}$) for $\boldsymbol{q}_C = (0.2a^*,\ 0,\ 0)$ in $NdNiO_2$ in the $k_z = 0$ plane. Heatmaps are given in the same scale as those for $\boldsymbol{q}_A = (0.22a^*,\ 0.22b^*,\ 0)$.

$$H_2 = t_1^{\mathrm{Nd}}\left[\sum_{i\tau_1\sigma} a_{i\sigma}^{\dagger} a_{i+\tau_1\sigma}\right] + t_2^{\mathrm{Nd}}\left[\sum_{i\tau_2\sigma} a_{i\sigma}^{\dagger} a_{i+\tau_2\sigma}\right] + t_3^{\mathrm{Nd}}\left[\sum_{i\tau_3\sigma} a_{i\sigma}^{\dagger} a_{i+\tau_3\sigma}\right],$$

$$H_3 = t_1^{\mathrm{Ni}}\left[\sum_{i\tau_1\sigma} b_{i\sigma}^{\dagger} b_{i+\tau_1\sigma}\right] + t_2^{\mathrm{Ni}}\left[\sum_{i\tau_2\sigma} b_{i\sigma}^{\dagger} b_{i+\tau_2\sigma}\right] + t_3^{\mathrm{Ni}}\left[\sum_{i\tau_3\sigma} b_{i\sigma}^{\dagger} b_{i+\tau_3\sigma}\right],$$

$$H_4 = U\sum_i n_{bi\uparrow} n_{bi\downarrow} + \mu\sum_{i\sigma}[(1+\Delta/\mu)n_{ai\sigma} + n_{bi\sigma}],$$

$$H_5 = V\sum_i n_{bi} n_{b(i+\tau_1)}. \qquad \text{(A1)}$$

Here, $a_{i\sigma}$ ($b_{i\sigma}$) and $a_{i\sigma}^{\dagger}$ ($b_{i\sigma}^{\dagger}$) are annihilation and creation operators of electrons at sites $\boldsymbol{R_i}$ with spin σ ($\sigma = \uparrow, \downarrow$) on sublattice A (B). The electronic number operator at sites $\boldsymbol{R_i}$ with spin σ on sublattice A (B) is $n_{ai\sigma} = a_{i\sigma}a_{i\sigma}^{\dagger}$ ($n_{bi\sigma} = b_{i\sigma}b_{i\sigma}^{\dagger}$). The t_1, t_2, and t_3 are hopping parameters between nearest-, next-nearest-, and third-nearest-neighbor sites, which are extracted from the DFT calculations (Table I). The relative positions are $\eta = (\pm 3\hat{x},\ \pm 3\hat{y})$, $\tau_1 = (\pm 2\hat{x},\ 0)$ and $(0,\ \pm 2\hat{y})$, $\tau_2 = (\pm 2\hat{x},\ \pm 2\hat{y})$, and $\tau_3 = (\pm 4\hat{x},\ 0)$ and $(0,\ \pm 4\hat{y})$. U is the on-site Coulomb interaction of the Ni $3d_{x2-y2}$ orbital, μ is the chemical potential of the Ni $3d$ orbit, and Δ is the on-site energy difference between Nd $5d$ and Ni $3d$ orbitals. V is the nearest-neighbor repulsion of the Ni $3d$ orbital. To simplify the calculations, the d-p type interaction is absent in our current paper. The density-density correlation function is used to characterize the CDW order:

$$C(R) = \frac{1}{N_s N_R}\sum_i \sum_{|j-i|=R} \langle (n_i - \langle n_i\rangle)(n_j - \langle n_j\rangle)\rangle, \qquad \text{(A2)}$$

where N_R is the distance between the site $\boldsymbol{R_i}$ and $\boldsymbol{R_j}$. The distance between site i and site j is R. The N_R is the amount of distance R. The Fourier transform is

$$C(q) = \frac{1}{N_s}\sum_R e^{iqR} C(R). \qquad \text{(A3)}$$

The simulated lattice for $NdNiO_2$ is shown in Fig. 19(a). Figure 19(b) gives the density-density correlations C® versus the distances R for different nearest-neighbor repulsion V at half filling $\langle n\rangle = 1.0$ (corresponding to the undoped case) and temperature $T = t/6$ ($t = |t_1| = -0.317$ eV is the nearest-neighbor hopping of Ni $3d$). A staggered pattern can be clearly identified with the interaction strength increasing to $V = 0.9t$, supporting the development of the CDW state. In Fig. 19(c), the density-density correlations $C(q)$ peak at $q = (\pi, \pi)$ with minor size-dependency, indicating a checkboard type CDW [charge order modulation along the (h, h) direction]. Test calculation for different T [Fig. 20(a)] shows identical patterns with small dropping at (π, π) with the increasing of temperature. Because of the sign problem, results are unreliable at lower temperatures or higher interactions. Based on the multiband Hubbard model on a two-dimensional square lattice under periodic boundary conditions, our unbiased numerical results indicate it may develop a charge order modulation along the (h, h) direction, much different from the charge modulation along the $(h, 0)$ direction observed in experiment. For the DQMC method, the notorious sign problem prevents accurate results for higher interaction, larger lattice, and lower temperature. To ensure the reliability of our simulations, we complement the average sign in Fig. 20(b)

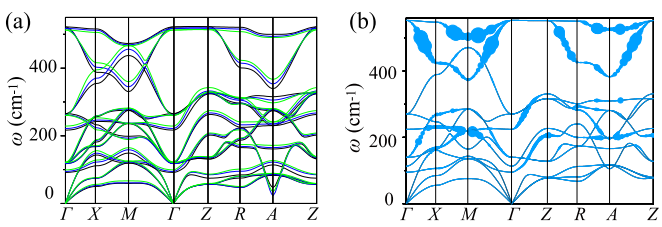

FIG. 27. (a) Calculated phonon spectra of $NdNiO_2$ as functions of hole doping. Black, blue, and green lines are results under $n_h = 0.0$, 0.1, and 0.2 Sr/u.c., respectively. (b) Phonon spectrum of undoped $LaNiO_2$ with line thickness indicating the magnitude of phonon linewidth.

TABLE I. Hopping parameters for two orbitals (Nd $5d_{z2}$ and Ni $3d_{x2-y2}$), obtained from DFT+Wannier downfolding of $NdNiO_2$.

	t^{Nd}			t^{Ni}			$t^{\mathrm{Nd-Ni}}$
	t_1	t_2	t_3	t_1	t_2	t_3	t_3
Hopping (eV)	–0.003	–0.157	0.001	–0.317	0.050	–0.055	0.021

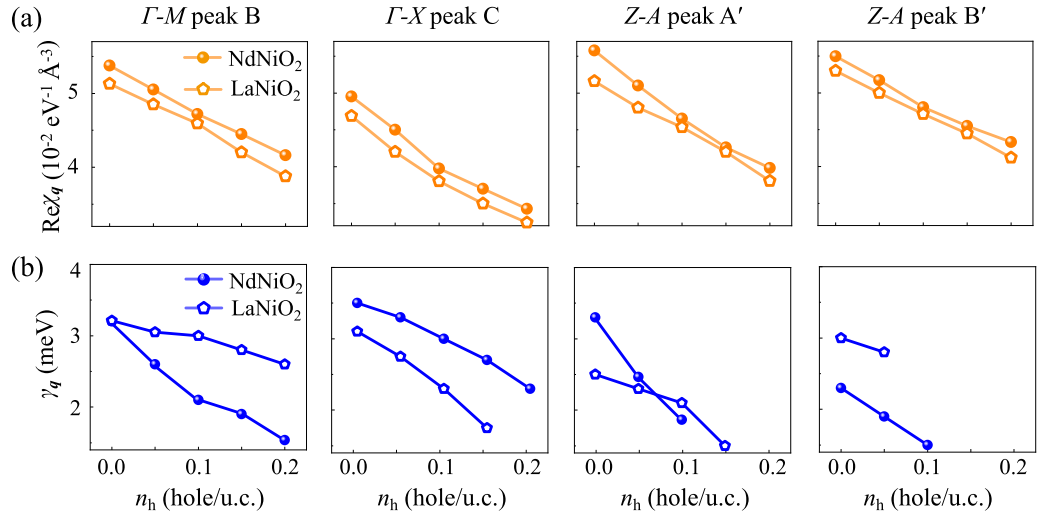

FIG. 28. Comparison of (a) DMFT static-QP Re$\chi_{\boldsymbol{q}}$ and (b) DFT-calculated $\gamma_{\boldsymbol{q}}$ for $NdNiO_2$ and $LaNiO_2$ as functions of n_h for other peaks.

for various parameters such as interaction, temperature, and lattice size with the Monte Carlo parameters of 10 000 runs. Our numerical results are reliable as the average sign is mostly larger than 0.50 even for the $V = 0.9t$, $T = t/6$, and $L = 12$ with 10000 runs measurements. For the presence of sign problem, much longer measurements are necessary to keep the same quality of data with $\langle \text{sign} \rangle \approx 1$. In our calculations, some of the results are obtained with more than 40 000 runs to compensate the fluctuations.

4. Hole doping dependent MEPC

The features of n_h-dependent $\gamma(\boldsymbol{q})$ are similar in $LaNiO_2$ (Fig. 21) and $NdNiO_2$ (Fig. 3 in main text). When $n_h = 0$, the $\boldsymbol{q}$ for generating high-intensity peaks in $\gamma(\boldsymbol{q})$ are generally consistent with that in Re$\chi(\boldsymbol{q})$ (Fig. 12), although the relative intensities for different peaks are slightly different in these two spectra. Remarkably, when n_h increases, the intensities of these peaks dramatically decrease, and some of them (e.g., A' and B') can even disappear at a high n_h. In addition, the basic features of n_h-dependent $\gamma(\boldsymbol{q})$ exist at different choices of U (Figs. 22 and 23) for the DFT calculations. Again, the wave vectors $\boldsymbol{q}$ at the maximum are very identical in $NdNiO_2$ and $LaNiO_2$, not only in the parent phase but even in the hole doping case for both $U = 0$ and 6 eV.

The MEPC features in $CaCuO_2$ (Fig. 24) are quite different from that in $NdNiO_2$.

(1) In contrast to $NdNiO_2$, the peak positions in $\gamma(\boldsymbol{q})$ are inconsistent with that in Re$\chi(\boldsymbol{q})$ (Fig. 13).

(2) The $\gamma(\boldsymbol{q})$ of $CaCuO_2$ are very insensitive to n_h, which is inconsistent with the experimentally observed n_h-dependent CDW formation in cuprates.

Figure 4(a) in the main text shows the orbital- and $\boldsymbol{k}$-resolved g($\boldsymbol{k}$) for the sum of all phonon modes which highlights the important contribution of the intraband scattering of the Nd $5d_{z^2}$ orbital. The interband scattering between Ni $3d_{x2-y2}$ and Nd $5d_{z^2}$ orbitals shown in Fig. 25 is in the same magnitude as the intraband scattering of the Ni $3d_{x2-y2}$ orbital and is $\approx 50\%$ smaller than the intraband scattering of the Nd $5d_{z^2}$ orbital. The orbital- and k- resolved $g(\boldsymbol{k})$ for the peak of $\boldsymbol{q}_C$ along the G-X line in the $k_z = 0$ plane (see Fig. 3 in the main text) are given in Fig. 26. The overall values are smaller than those for the $\boldsymbol{q}_A$ point. The major contributions to g($\boldsymbol{k}$) come from intraband scattering of the Nd $5d_{z^2}$ orbital.

As shown in Fig. 27(a), with increasing n_h, the phonon spectrum of $NdNiO_2$ only has small changes. Some phonon modes slightly change upon doping, e.g., the optical mode around 400 cm^{-1} is enhanced to higher frequency due to decoupling to Nd orbitals. The phonon spectrum as well as its linewidth of $LaNiO_2$ given in Fig. 27(b) is similar to that of $NdNiO_2$ [Fig. 4(b) in the main text].

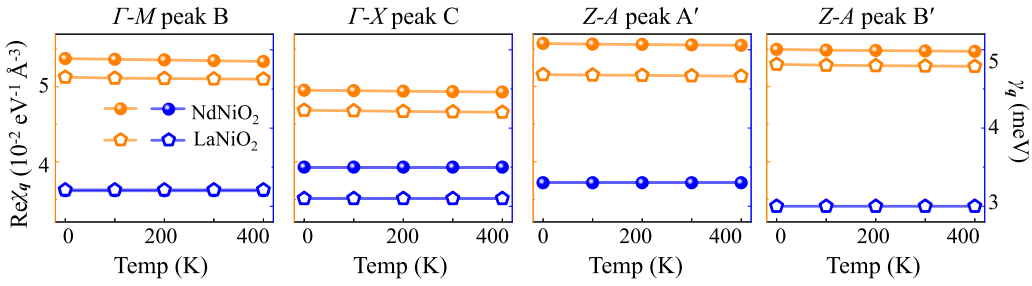

FIG. 29. DMFT static-QP Re$\chi_{\boldsymbol{q}}$ and DFT-calculated $\gamma_{\boldsymbol{q}}$ as functions of temperature for other peaks.

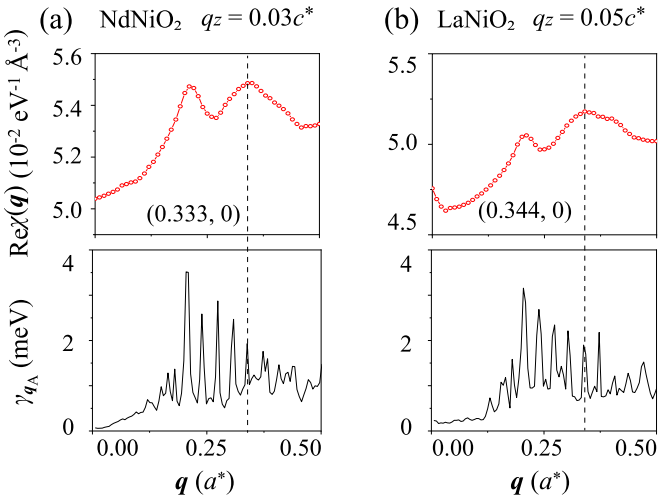

FIG. 30. (a) Experimentally measured $\boldsymbol{q}_{\mathrm{CDW}}$ can be peaked in the calculated $\mathrm{Re}\chi(\boldsymbol{q})$ (upper panel) and $\gamma(\boldsymbol{q})$ (bottom panel) at different q_z in (a) $NdNiO_2$ and (b) $LaNiO_2$.

5. Comparison between $NdNiO_2$ and $LaNiO_2$

In Fig. 5 of the main text, we show that the values of $\mathrm{Re}\chi_{\boldsymbol{q}A}$ and $\gamma_{\boldsymbol{q}A}$ in $LaNiO_2$ are smaller than that of $NdNiO_2$, and both gradually decrease with n_h, accompanied by the decreases of $\boldsymbol{q}_A$. Figure 28 gives the values of $\mathrm{Re}\chi(\boldsymbol{q})$ and $\gamma(\boldsymbol{q})$ for other peaks. The trend and their hole doping dependent behaviors are similar to those for peak A. Moreover, the calculated values of $\mathrm{Re}\chi_{\boldsymbol{q}A}$ and $\gamma_{\boldsymbol{q}A}$ are insensitive to the temperature at least up to 400 K for undoped $R\mathrm{NiO}_2$ (Fig. 29).

6. Comparison between theory and experimental observations

As shown in Fig. 30, by assuming a specific q_z ($q_z = 0.03c^*$ and $0.05c^*$ for $NdNiO_2$ and $LaNiO_2$), we can clearly identify the peaks at (0.333, 0) in $NdNiO_2$ and at (0.344, 0) in $LaNiO_2$ in both $\mathrm{Re}\chi(\boldsymbol{q})$ and $\gamma(\boldsymbol{q})$ spectra, which may trigger the experimentally observed CDW with $\boldsymbol{q}_{\mathrm{CDW}}$ at (0.333, 0) in $NdNiO_2$ and at (0.344, 0) in $LaNiO_2$, respectively. Again, our calculations not only indicate that a joint EI and MEPC is important for CDW formation in nickelates, but also predicts that the $\boldsymbol{q}_{\mathrm{CDW}}$ in $LaNdO_2$ and $NdNiO_2$ could be very similar due to their nearly identical peaks in $\mathrm{Re}\chi(\boldsymbol{q})$ and $\gamma(\boldsymbol{q})$, consistent with the experimental observations.

[1] J. G. Bednorz and K. A. Müller, Possible high T_c superconductivity in the Ba−La−Cu−O system, Z. Phys. B **64**, 189 (1986).

[2] M. Azuma, Z. Hiroi, M. Takano, Y. Bando, and Y. Taketa, Superconductivity at 110 K in the infinite-layer compound $(Sr_{1-x}Ca_x)_{1-y}CuO_2$, Nature (London) **356**, 775 (1992).

[3] N. Damascelli, Z. Hussain, and Z.-X. Shen, Angle-resolved photoemission studies of the cuprate superconductors, Rev. Mod. Phys. **75**, 473 (2003).

[4] E. Fradkin, S. A. Kivelson, and J. M.Tranquada, Theory of intertwined orders in high temperature superconductors, Rev. Mod. Phys. **87**, 457 (2015).

[5] R. Comin and A. Damascelli, Resonant x-ray scattering studies of charge order in cuprates, Annu. Rev. Condens. Matter Phys. **7**, 369 (2016).

[6] V. I. Anisimov, D. Bukhvalov, and T. M. Rice, Electronic structure of possible nickelate analogs to the cuprates, Phys. Rev. B **59**, 7901 (1999).

[7] M. A. Hayward, M. A. Green, M. J. Rosseinsky, and J. Sloan, Sodium hydride as a powerful reducing agent for topotactic oxide deintercalation: Synthesis and characterization of the nickel(I) oxide $LaNiO_2$, J. Am. Chem. Soc. **121**, 8843 (1999).

[8] D. Li, K. Lee, B. Y. Wang, M. Osada, S. Crossley, H. R. Lee, Y. Cui, Y. Hikita, and H. Y. Hwang, Superconductivity in an infinite-layer nickelate, Nature (London) **572**, 624 (2019).

[9] M. Osada, B. Y. Wang, Be. H. Goodge, S. P. Harvey, K. O. Lee, D. Li, L. F. Kourkoutis, and H. Y. Hwang, Nickelate superconductivity without rare-earth magnetism: $(La, Sr)NiO_2$, Adv. Mater. **33**, 45 (2021).

[10] M. Osada, B. Y. Wang, B. H. Goodge, K. Lee, H. Yoon, K. Sakuma, D. Li, M. Miura, L. F. Kourkoutis, and H. Y. Hwang, A superconducting praseodymium nickelate with infinite layer structure, Nano Lett. **20**, 5735 (2020).

[11] G. A. Pan, D. F. Segedin, H. LaBollita, Q. Song, E. M. Nica, B. H. Goodge, A. T. Pierce, S. Doyle, S. Novakov, D. C. Carrizales, A. T. N' Diaye, P. Shafer, H. Paik, J. T. Heron, J. A. Mason, A. Yacoby, L. F. Kourkoutis, O. Erten, C. M. Brooks, A. S. Botana, and J. A. Mundy, Superconductivity in a quintuple-layer square planar nickelate, Nat. Mater. **21**, 160 (2022).

[12] F. Lechermann, Multiorbital Processes Rule the $Nd_{1-x}Sr_xNiO_2$ Normal State, Phys. Rev. X **10**, 041002 (2020).

[13] J. Karp, A. S. Botana, M. R. Norman, H. Park, M. Zing, and A. Millis, Many-Body Electronic Structure of $NdNiO_2$ and $CaCuO_2$, Phys. Rev. X **10**, 021061 (2020).

[14] A. S. Botana1 and M. R. Norman, Similarities and Differences between $LaNiO_2$ and $CaCuO_2$ and Implications for Superconductivity, Phys. Rev. X **10**, 011024 (2020).

[15] D. C. Peets, D. G. Hawthorn, K. M. Shen, Young-June Kim, D. S. Ellis, H. Zhang, Seiki Komiya, Yoichi Ando, G. A. Sawatzky, Ruixing Liang, D. A. Bonn, and W. N. Hardy, X-Ray Absorption Spectra Reveal the Inapplicability of the Single-Band Hubbard Model to Overdoped Cuprate Superconductors, Phys. Rev. Lett. **103**, 087402 (2009).

[16] H. Sakakibara, H. Usui, K. Kuroki, R. Arita, and H. Aoki, Two-Orbital Model Explains The Higher Transition Temperature of the Single-Layer Hg-Cuprate Superconductor Compared to that of the La-Cuprate Superconductor, Phys. Rev. Lett. **105**, 057003 (2010).

[17] Y. Nomura, M. Hirayama, T. Tadano, Y. Yoshimoto, K. Nakamura, and R. Arita, Formation of a two-dimensional single-component correlated electron system and band engineering in the nickelate superconductor $NdNiO_2$, Phys. Rev. B **100**, 205138 (2019).

[18] H. LaBollita and A. S. Botana, Correlated electronic structure of a quintuple-layer nickelate, Phys. Rev. B **105**, 085118 (2022).

[19] K. McElroy, D.-H. Lee, J. E. Hoffman, K. M. Lang, J. Lee, E. W. Hudson, H. Eisaki, S. Uchida, and J. C. Davis, Coincidence of Checkerboard Charge Order and Antinodal State Decoherence In Strongly Underdoped Superconducting $Bi_2Sr_2CaCu_2O_8$, Phys. Rev. Lett. **94**, 197005 (2005).

[20] J. Chang, E. Blackburn, A. T. Holmes, N. B. Christensen, J. Larsen, J. Mesot, Ruixing Liang, D. A. Bonn, W. N. Hardy, A. Watenphul, M. v. Zimmermann, E. M. Forgan, and S. M. Hayden, Direct observation of competition between superconductivity and charge density wave order in $YBa_2Cu_3O_{6.67}$, Nat. Phys. **8**, 871 (2012).

[21] M. Rossi, M. Osada, J. Choi, S. Agrestini, D. Jost, Y. Lee, H. Lu, B. Y. Wang, K. Lee, A. Nag, Y.-D. Chuang, K. C.-T., S.-J. Lee, B. Moritz, T. P. Devereaux, Z.-X. Shen, J.-S. Lee, K.-J. Zhou, H. Y. Hwang, and W.-S. Lee, A broken translational symmetry state in an infinite-layer nickelate, Nat. Phys. **18**, 869 (2022).

[22] C. C. Tam, J. Choi, X. Ding, S. Agrestini, A. Nag, B. Huang, H. Luo, M. G.-Fernández, L. Qiao, and K.-J. Zhou, Charge density waves in infinite-layer $NdNiO_2$ nickelates, Nat. Mater. **21**, 1116 (2022).

[23] G. Krieger, L. Martinelli, S. Zeng, L. E. Chow, K. Kummer, R. Arpaia, M. Moretti Sala, N. B. Brookes, A. Ariando, N. Viart, M. Salluzzo, G. Ghiringhelli, and D. Preziosi, Charge and Spin Order Dichotomy in $NdNiO_2$ Driven by $SrTiO_3$ Capping Layer, Phys. Rev. Lett. **129**, 027002 (2022).

[24] S. Badoux, S. A. A. Afshar, B. Michon, A. Ouellet, S. Fortier, D. LeBoeuf, T. P. Croft, C. Lester, S. M. Hayden, H. Takagi, K. Yamada, D. Graf, N. Doiron-Leyraud, and L. Taillefer, Critical Doping for the Onset of Fermi-Surface Reconstruction by Charge-Density-Wave Order in the Cuprate Superconductor $La_{2-x}Sr_xCuO_4$, Phys. Rev. X **6**, 021004 (2016).

[25] R. Raimondi, C. Castellani, and M. Grilli, Charge collective modes and dynamic pairing in the three-band Hubbard model. II. Strong-coupling limit, Phys. Rev. B **47**, 3331 (1993).

[26] A. Lanzara, P. V. Bogdanov, X. J. Zhou, S. A. Kellar, D. L. Feng, E. D. Lu, T. Yoshida, H. Eisaki, A. Fujimori, K. Kishio, J.-I. Shimoyama, T. Noda, S. Uchida, Z. Hussain, and Z.-X. Shen, Evidence for ubiquitous strong electron-phonon coupling in high-temperature superconductors, Nature (London) **412**, 510 (2001).

[27] P. Zhang, S. G. Louie, and M. L. Cohen, Electron-Phonon Renormalization in Cuprate Superconductors, Phys. Rev. Lett. **98**, 067005 (2007).

[28] Y. Y. Peng, A. A. Husain, M. Mitrano, S. X.-L. Sun, T. A. Johnson, A. V. Zakrzewski, G. J. MacDougall, A. Barbour, I. Jarrige, V. Bisogni, and P. Abbamonte, Enhanced Electron-Phonon Coupling for Charge-Density-Wave Formation in $La_{1.8-x}Eu_{0.2}Sr_xCuO_{4+\delta}$, Phys. Rev. Lett. **125**, 097002 (2020).

[29] C. C. Tam, M. Zhu, J. Ayres, K. Kummer, F. Yakhou-Harris, J. R. Cooper, A. Carrington, and S. M. Hayden, Charge density waves and Fermi surface reconstruction in the clean overdoped cuprate superconductor $Tl_2Ba_2CuO_{6+\delta}$, Nat. Commun. **13**, 570 (2022).

[30] E. W. Huang, C. B. Mendl, H.-C. Jiang, B. Moritz, and T. P. Devereaux, Stripe order from the perspective of the Hubbard model, npj Quantum Mater. **3**, 22 (2018).

[31] B.-X. Zheng, C.-M. Chung, P. Corboz, G. Ehlers, M.-P. Qin, R. M. Noack, H. Shi, S. R. White, S. Zhang, and G. K.-Lic Chan, Stripe order in the underdoped region of the two-dimensional Hubbard model, Science **358**, 1155 (2017).

[32] E. W. Huang, C. B. Mend, Shenxiu Liu, S. Johnston, H.-C. Jiang, B. Moritz, and T. P. Devereaux, Numerical evidence of fluctuating stripes in the normal state of high-T_c cuprate superconductors, Science **358**, 1161 (2017).

[33] T. Zhou, Y. Gao, and Z. Wang, Spin excitations in nickelate superconductors, Sci. China Phys. Mech. Astron. **63**, 287412 (2020).

[34] S. Huangfu, Z. Guguchia, D. Cheptiakov, X. Zhang, H. Luetkens, D. J. Gawryluk, T. Shang, F. O. von Rohr, and A. Schilling, Short-range magnetic interactions and spin-glass behavior in the quasi-two-dimensional nickelate $Pr_4Ni_3O_8$, Phys. Rev. B **102**, 054423 (2020).

[35] H. Lu, M. Rossi, A. Nag, M. Osada, D. F. Li, K. Lee, B. Y. Wang, M. Garcia-Fernandez, S. Agrestini, Z. X. Shen, E. M. Been, B. Moritz, T. P. Devereaux, J. Zaanen, H. Y. Hwang, Ke-Jin Zhou, and W. S. Lee, Magnetic excitations in infinite-layer nickelates, Science **373**, 213 (2021).

[36] A. Ricci, N. Poccia, G. Campi, S. Mishra, L. Müller, B. Joseph, B. Shi, A. Zozulya, M. Buchholz, C. Trabant, J. C. T. Lee, J. Viefhaus, J. B. Goedkoop, A. A. Nugroho, M. Braden, S. Roy, M. Sprung, and C. Schüßler-Langeheine, Measurement of Spin Dynamics in a Layered Nickelate Using X-Ray Photon Correlation Spectroscopy: Evidence for Intrinsic Destabilization of Incommensurate Stripes at Low Temperatures, Phys. Rev. Lett. **127**, 057001 (2021).

[37] X. Zhou, X. Zhang, J. Yi, P. Qin, Z. Feng, P. Jiang, Z. Zhong, H. Yan, X. Wang, H. Chen, H. Wu, X. Zhang, Z. Meng, X. Yu, M. B. H. Breese, J. Cao, J. Wang, C. Jiang, and Z. Liu, Antiferromagnetism in Ni-based superconductors, Adv. Mater. **34**, 2106117 (2022).

[38] Y. Gu, S. Zhu, X. Wang, J. Hu, and H. Chen, A substantial hybridization between correlated Ni-d orbital and itinerant electrons in infinite-layer nickelates, Commun. Phys. **3**, 84 (2020).

[39] I. Leonov, Effect of lattice strain on the electronic structure and magnetic correlations in infinite-layer (Nd, Sr)NiO_2, J. Alloys Compd. **883**, 160888 (2021).

[40] B. Kang, C. Melnick, P. Semon, S. Ryee, M. J. Han, G. Kotliar, and S. Choi, Infinite-layer nickelates as Ni-eg Hund's metals, arXiv:2007.14610 (2021).

[41] Y. Wang, C.-J. Kang, H. Miao, and G. Kotliar, Hund's metal physics: From $SrNiO_2$ to $LaNiO_2$, Phys. Rev. B **102**, 161118(R) (2020).

[42] M. Kitatani, L. Si, O. Janson, R. Arita, Z. Zhong, and K. Held, Nickelate superconductors-a renaissance of the one-band Hubbard model, npj Quantum. Mater. **5**, 59 (2020).

[43] C. Weber, K. Haule, and G. Kotliar, Strength of correlations in electron- and hole-doped cuprates, Nat. Phys. **6**, 574 (2010).

[44] H. Kajueter, G. Kotliar, and G. Moeller, Doped Mott insulator: Results from mean-field theory, Phys Rev. B **53**, 16214 (1996).

[45] D. J. García, E. Miranda, K. Hallberg, and M. J. Rozenberg, Mott transition in the Hubbard model away from particle-hole symmetry, Phys. Rev. B **75**, 121102(R) (2007).

[46] E. Been, W.-S. Lee, H. Y. Hwang, Y. Cui, J. Zaanen, T. Devereaux, B. Moritz, and C. Jia, Electronic Structure Trends Across the Rare-Earth Series in Superconducting Infinite-Layer Nickelates, Phys. Rev. X **11**, 011050 (2021).

[47] H. Sakakibara, H. Usui, K. Suzuki, T. Kotani, H. Aoki, and K. Kuroki, Model Construction and a Possibility of Cupratelike Pairing in a New d^9 Nickelate Superconductor (Nd, Sr)NiO_2, Phys. Rev. Lett. **125**, 077003 (2020).

[48] P. Jiang, L. Si, Z. Liao, and Z. Zhong, Electronic structure of rare-earth infinite-layer $RNiO_2$ (R = La, Nd), Phys. Rev. B **100**, 201106(R) (2019).

[49] K.-W. Lee and W. E. Pickett, Infinite-layer $LaNiO_2$: Ni^{1+} is not Cu^{2+}, Phys. Rev. B **70**, 165109 (2004).

[50] M.-Y. Choi, K.-W. Lee, and W. E. Pickett, Role of 4f states in infinite-layer $NdNiO_2$, Phys. Rev. B **101**, 020503(R) (2020).

[51] Z. Liu, C. Xu, C. Cao, W. Zhu, Z. F. Wang, and J. Yang, Doping dependence of electronic structure of infinite-layer $NdNiO_2$, Phys. Rev. B **103**, 045103 (2021).

[52] P. A. Lee, N. Nagaosa, and X-G. Wen, Doping a Mott insulator: Physics of high-temperature superconductivity, Rev. Mod. Phys. **78**, 17 (2006).

[53] P. Cai, W. Ruan, Y. Peng, C. Ye, X. Li, Z. Hao, X. Zhou, D.-H. Lee, and Y. Wang, Visualizing the evolution from the Mott insulator to a charge-ordered insulator in lightly doped cuprates, Nat. Phys. **12**, 1047 (2016).

[54] S. Badoux, W. Tabis, F. Laliberté, G. Grissonnanche, B. Vignolle, D. Vignolles, J. Béard, D. A. Bonn, W. N. Hardy, R. Liang, N. D.-Leyraud, L. Taillefer, and C. Proust, Change of carrier density at the pseudogap critical point of a cuprate superconductor, Nature (London) **531**, 210 (2016).

[55] J. G. Si, W. J. Lu, H. Y. Wu, H. Y. Lv, X. Liang, Q. J. Li, and Y. P. Sun, Origin of the multiple charge density wave order in 1T-VSe_2, Phys. Rev. B **101**, 235405 (2020).

[56] R. Blankenbecler, D. J. Scalapino, and R. L. Sugar, Monte Carlo calculations of coupled boson-fermion systems, I. Phys. Rev. D **24**, 2278 (1981).

[57] S. Zhang, Finite-Temperature Monte Carlo Calculations for Systems with Fermions, Phys. Rev. Lett. **83**, 2777 (1999).

[58] T. Ma, H.-Q. Lin, and J. Hu, Quantum Monte Carlo Study of a Dominant S-Wave Pairing Symmetry in Iron-Based Superconductors, Phys. Rev. Lett. **110**, 107002 (2013).

[59] R. Mondaini1, S. Taratl, and R. T. Scalettar, Quantum critical points and the sign problem, Science **375**, 418 (2022).

[60] Zhua X, Y. Cao, J. Zhang, E. W. Plummerb, and J. Guo, Classification of charge density waves based on their nature, Proc. Natl. Acad. Sci. USA **112**, 2367 (2015).

[61] D. Reznik, L. Pintschovius, M. Ito, S. Iikubo, M. Sato, H. Goka, M. Fujita, K. Yamada, G. D. Gu, and J. M. Tranquada, Electron-phonon coupling reflecting dynamic charge inhomogeneity in copper oxide superconductors, Nature (London) **440**, 1170 (2006).

[62] M. L. Tacon, A. Bosak, S. M. Souliou, G. Dellea, T. Loew, R. Heid, K-P. Bohnen, G. Ghiringhelli, M. Krisch, and B. Keimer, Inelastic x-ray scattering in $YBa_2Cu_3O_{6.6}$ reveals giant phonon anomalies and elastic central peak due to charge-density-wave formation, Nat. Phys. **10**, 52 (2014).

[63] H. Miao, D. Ishikawa, R. Heid, M. Le Tacon, G. Fabbris, D. Meyers, G. D. Gu, A. Q. R. Baron, and M. P. M. Dean, Incommensurate Phonon Anomaly and the Nature of Charge Density Waves in Cuprates, Phys. Rev. X **8**, 011008 (2018).

[64] M. Raichle, D. Reznik, D. Lamago, R. Heid, Y. Li, M. Bakr, C. Ulrich, V. Hinkov, K. Hradil, C. T. Lin, and B. Keimer, Highly Anisotropic Anomaly in the Dispersion of the Copper-Oxygen Bond-Bending Phonon in Superconducting $YBa_2Cu_3O_7$ from Inelastic Neutron Scattering, Phys. Rev. Lett. **107**, 177004 (2011).

[65] C. Gros and R. Werner, Dynamics of the Peierls-active phonon modes in $CuGeO_3$, Phys. Rev. B **58**, R14677(R) (1998).

[66] M. Holicki, H. Fehske, and R. Werner, Magnetoelastic excitations in spin-Peierls systems, Phys. Rev. B **63**, 174417 (2001).

[67] F. Ye, G.-H. Ding, and B.-W. Xu, Dynamical properties of phonons in the XY spin chain coupled with lattices, Phys. Rev. B **64**, 094431 (2001).

[68] Z. Li and S. G. Louie, Two-gap superconductivity and decisive role of rare-earth d electrons in infinite-layer nickelates, arXiv:2210.12819.

[69] L. Si, W. Xiao, J. Kaufmann, J. M. Tomczak, Y. Lu, Z. Zhong, and K. Held, Topotactic Hydrogen in Nickelate Superconductors and Akin Infinite-Layer Oxides ABO_2, Phys. Rev. Lett. **124**, 166402 (2020).

[70] B. H. Goodge, B. Geisler, K. Lee, M. Osada, B. Y. Wang, D. Li, H. Y. Hwang, R. Pentcheva, and L. F. Kourkoutis, Reconstructing the polar interface of infinite-layer nickelate thin films, arXiv:2201.03613.

[71] G. Paolo, B. Stefano, B. Nicola, C. Matteo, C. Roberto, C. Carlo, C. Davide, L. C. Guido, C. Matteo, D. Ismaila, C. AndreaDal, G. Stefano de, F. Stefano, F. Guido, G. Ralph, G. Uwe, G. Christos, K. Anton, L. Michele, M.-S. Layla, M. Nicola, M. Francesco, M. Riccardo, P. Stefano, P. Alfredo, P. Lorenzo, S. Carlo, S. Sandro, S. Gabriele, P. S. Ari, S. Alexander, U. Paolo, and M. W. Renata, QUANTUM ESPRESSO: A modular and open-source software project for quantum simulations of materials, J. Phys.: Condens. Matter **21**, 395502 (2009).

[72] D. Vanderbilt, Soft self-consistent pseudopotentials in a generalized eigenvalue formalism, Phys. Rev. B **41**, 7892 (1990).

[73] G. Kresse and J. Furthmüller, Efficient iterative schemes for *ab initio* total-energy calculations using a plane-wave basis set, Phys. Rev. B **54**, 11169 (1996).

[74] P. E. Blöchl, Projector augmented-wave method, Phys. Rev. B **50**, 17953 (1994).

[75] J. P. Perdew, K. Burke, and M. Ernzerhof, Generalized Gradient Approximation Made Simple, Phys. Rev. Lett. **77**, 3865 (1996).

[76] S. Grimme, J. Antony, S. Ehrlich, and S. Krieg, A consistent and accurate *ab initio* parametrization of density functional dispersion correction (DFT-D) for the 94 elements H-Pu, J. Chem. Phys. **132**, 154104 (2010).

[77] S. Baroni, S. De Gironcoli, A. Dal Corso, and P. Giannozzi, Phonons and related crystal properties from density-functional perturbation theory, Rev. Mod. Phys. **73**, 515 (2001).

[78] F. Giustino, M. L. Cohen, and S. G. Louie, Electron-phonon interaction using Wannier functions, Phys. Rev. B **76**, 165108 (2007).

[79] S. Poncé, E. R. Margine, C. Verdi, and F. Giustino, EPW: Electron-phonon coupling, transport and superconducting properties using maximally localized Wannier functions, Comput. Phys. Commun. **209**, 116 (2016).

[80] V. Anisimov, J. Zaanen I., and O. K. Anderson, Band theory and Mott insulators: Hubbard U instead of Stoner I, Phys. Rev. B **44**, 943 (1991).

[81] V. I. Anisimov, A. I. Poteryaev, M. A. Korotin, A. O. Anokhin, and G. Kotlia, First-principles calculations of the electronic

structure and spectra of strongly correlated systems: Dynamical mean-field theory, J. Phys.: Condens. Matter **9**, 7359 (1997).

[82] L. Bellaiche and D. Vanderbilt, Virtual crystal approximation revisited: Application to dielectric and piezoelectric properties of perovskites, Phys. Rev. B **61**, 7877 (2000).

[83] P. Blaha, K. Schwarz, F. Tran, R. Laskowski, G. K. H. Madsen, and L. D. Marks, WIEN2k: An APW+lo program for calculating the properties of solids, J. Chem. Phys. **152**, 074101 (2020).

[84] M. Hepting, D. Li, C. J. Jia, H. Lu, E. Paris, Y. Tseng, X. Feng, M. Osada, E. Been, Y. Hikita, Y.-D. Chuang, Z. Hussain, K. J. Zhou, A. Nag, M. Garcia-Fernandez, M. Rossi, H. Y. Huang, D. J. Huang, Z. X. Shen, T. Schmitt, H. Y. Hwang, B. Moritz, J. Zaanen, T. P. Devereaux, and W. S. Lee, Electronic structure of the parent compound of superconducting infinite-layer nickelates, Nat. Mater. **19**, 381 (2020).

[85] Z. Chen, M. Osada, D. Li, E. M. Been, S.-D. Chen, M. Hashimoto, D. Lu, S.-K. Mo, K. Lee, Bai Y. Wang, F. Rodolakis, J. L. McChesney, C. Jia, B. Moritz, T. P. Devereaux, H. Y. Hwang, and Z.-X. Shen, Electronic structure of superconducting nickelates probed by resonant photoemission spectroscopy, Matter **5**, 1806 (2022).

[86] E. Gull, A. J. Millis, A. I. Lichtenstein, A. N. Rubtsov, M. Troyer, and P. Werner, Continuous-time Monte Carlo methods for quantum impurity models, Rev. Mod. Phys. **83**, 349 (2011).

[87] M. D. Johannes and I. I. Mazin, Fermi surface nesting and the origin of charge density waves in metals, Phys. Rev. B **77**, 165135 (2008).

[88] Y.-X. Zhang, W.-T. Chiu, N. C. Costa, G. G. Batrouni, and R. T. Scalettar, Charge Order in the Holstein Model on a Honeycomb Lattice, Phys. Rev. Lett. **122**, 077602 (2019).

[89] N. C. Costa, K. Seki, S. Yunoki, and S. Sorella, Phase diagram of the two-dimensional Hubbard-Holstein model, Commun. Phys. **3**, 80 (2020).

[90] L. Wang, P. Corboz, and M. Troyer, Fermionic quantum critical point of spinless fermions on a honeycomb lattice, New J. Phys. **16**, 103008 (2014).

[91] Z.-X. Li, Y.-F. Jiang, and H. Yao, Solving the fermion sign problem in quantum Monte Carlo simulations by Majorana representation, Phys. Rev. B **91**, 241117 (2015).